

CERN-PH-EP-2014-254  
08 October 2014

3  
4

## Charged jet cross sections and properties in proton-proton collisions at $\sqrt{s} = 7$ TeV

5  
6

The ALICE Collaboration\*

7

### Abstract

8  
9  
10  
11  
12  
13  
14  
15  
16  
17  
18  
19  
20  
21

The differential charged jet cross sections, jet fragmentation distributions, and jet shapes are measured in minimum bias proton-proton collisions at centre-of-mass energy  $\sqrt{s} = 7$  TeV using the ALICE detector at the LHC. Jets are reconstructed from charged particle momenta in the mid-rapidity region using the sequential recombination  $k_T$  and anti- $k_T$  as well as the SISCone jet finding algorithms with several resolution parameters in the range  $R = 0.2 - 0.6$ . Differential jet production cross sections measured with the three jet finders are in agreement in the transverse momentum ( $p_T$ ) interval  $20 < p_T^{\text{jet, ch}} < 100$  GeV/c. They are also consistent with prior measurements carried out at the LHC by the ATLAS collaboration. The jet charged particle multiplicity rises monotonically with increasing jet  $p_T$ , in qualitative agreement with prior observations at lower energies. The transverse profiles of leading jets are investigated using radial momentum density distributions as well as distributions of the average radius containing 80% ( $\langle R_{80} \rangle$ ) of the reconstructed jet  $p_T$ . The fragmentation of leading jets with  $R = 0.4$  using scaled  $p_T$  spectra of the jet constituents is studied. The measurements are compared to model calculations from event generators (PYTHIA, PHOJET, HERWIG). The measured radial density distributions and  $\langle R_{80} \rangle$  distributions are well described by the PYTHIA model (tune Perugia-2011). The fragmentation distributions are better described by HERWIG.

---

\*See Appendix A for the list of collaboration members

## 1 Introduction

Jets consist of collimated showers of particles resulting from the fragmentation of hard (high momentum transfer  $Q$ ) partons (quarks and gluons) produced in high energy collisions. The production cross sections of jets were measured in detail in proton-antiproton ( $p\bar{p}$ ) collisions at the Tevatron ( $\sqrt{s} = 540$  GeV, 630 GeV, 1.8 TeV and 1.96 TeV) [1, 2]. Measurements were also carried out recently at the CERN LHC at higher energies ( $\sqrt{s} = 2.76$ , 7 and 8 TeV) in proton-proton (pp) collisions [3, 4, 5, 6]. Jet shape observables were previously measured by the CDF [7, 8, 9], and D0 [10] collaborations in  $p\bar{p}$  collisions and more recently by the ATLAS and CMS collaborations in pp collisions [11, 12, 13]. The fragmentation functions of jets produced in  $p\bar{p}$  collisions were reported by the CDF collaboration [14]. Jet fragmentation in pp and Pb–Pb collisions at the LHC were reported by the ATLAS [3, 15, 16] and CMS [17] collaborations. Jet production in  $e^+e^-$ , ep,  $p\bar{p}$ , and pp collisions is well described by perturbative Quantum Chromodynamics (pQCD) calculations. The measured jet properties are typically well reproduced by Monte Carlo (MC) generators such as PYTHIA [18], HERWIG [19], and PHOJET [20]. The unprecedented beam energy achieved at the Large Hadron Collider (LHC) in pp collisions enables an extension of jet production cross section and property measurements carried out at lower energies. Such measurements enable further tests of QCD and help in tuning of MC event generators.

In this paper, we present measurements of the jet production cross sections, jet fragmentation distributions, and transverse jet shape observables in pp collisions at  $\sqrt{s} = 7$  TeV. The analysis is restricted to charged particle jets, i.e. jets reconstructed solely from charged particle momenta, hereafter called charged jets. ALICE has already reported measurements of charged jet production in Pb–Pb collisions at 2.76 TeV [21]. Charged jets are reconstructed with particles having  $p_T$  down to values as low as 0.15 GeV/ $c$ , thereby allowing to test perturbative and non-perturbative aspects of jet production and fragmentation as implemented in MC generators. The measured particle spectra in jets reflect the jet fragmentation function, as summarized in [22] (Sec. 19). The jet shape distributions are related to the details of the parton shower process.

Jets also constitute an important probe for the study of the hot and dense QCD matter created in high energy collisions of heavy nuclei. In such collisions, large  $p_T$  partons penetrate the colored medium and lose energy via induced gluon radiation and elastic scattering (see [23] and references therein). The measurements in pp collisions thus provide a baseline for similar measurements in nucleus–nucleus (A–A) and proton-nucleus (p–A) collisions.

Medium modifications of the parton shower may change the fragmentation pattern relative to the vacuum [24]. There are empirical indications [25] that the scale relevant to these effects is given by the medium temperature of the order of few hundred MeV rather than the hard scattering scale. At such small particle momenta, the jets measured experimentally in pp and A–A collisions also contain contributions from the underlying event (UE). In pp collisions [8], the UE includes gluon radiation in the initial state, the fragmentation of beam remnants and multiple parton interactions. In this study, we subtract the UE from the distributions measured in pp collisions, to allow for a meaningful comparison to models, because theoretical modeling of the underlying event is very complex. To disentangle UE and hard parton fragmentation into low momentum particles, we correct our measurements using a technique similar to that applied in [14], described in Sec. 6.4. This approach will also help to make eventually a comparison with data from A–A collisions, where the UE in addition includes hadrons from an expanding fireball.

This paper is organized as follows. Section 2 describes the experiment and detectors used for the measurements reported in this work. Details of the jet reconstruction algorithms and parameters are presented in Sec. 3, while jet observables are defined and discussed in Sec. 4. Section 5 discusses the MC simulations carried out for comparisons of measured data to models, data corrections for instrumental effects, and systematic error studies. The procedures applied to correct for instrumental effects are presented in Sec. 6. The methods used to evaluate systematic uncertainties of the measurements are discussed

69 in Sec. 7. Results are presented and discussed in comparison with MC Event Generator simulations in  
 70 Sec. 8. Section 9 summarizes the results and conclusions of this work.

## 71 **2 Experimental setup and data sample**

72 The data used in this analysis were collected during the 2010 LHC run with the ALICE detector [26].  
 73 This analysis relies primarily on the Time Projection Chamber (TPC) [27], the Inner Tracking System  
 74 (ITS) [28], and the V0 [29] sub-detectors. The V0 and ITS are used for event selection. A minimum  
 75 bias trigger is achieved by requiring at least one hit in either the V0 forward scintillators or in the two  
 76 innermost Silicon Pixel Detector layers (SPD) of the ITS, in coincidence with an LHC bunch crossing.  
 77 The efficiency for detecting inelastic events is about 85% [30]. The TPC and ITS are used for primary  
 78 vertex and track reconstruction. Only events with a primary vertex within  $\pm 10$  cm along the beam direc-  
 79 tion from the nominal interaction point are analyzed to minimize dependencies of the TPC acceptance  
 80 on the vertex position. The results reported in this paper are based on  $177 \times 10^6$  minimum bias events  
 81 corresponding to an integrated luminosity [30] of  $(2.9 \pm 0.1) \text{ nb}^{-1}$ .

82 The ALICE solenoidal magnet is operated with a magnetic field of 0.5 T that provides a good compro-  
 83 mise between momentum resolution at high  $p_T$  and detection of low  $p_T$  particles. Charged tracks are  
 84 reconstructed using the combined information from the TPC and the ITS utilizing a hybrid reconstruc-  
 85 tion technique described in [6] to assure uniform  $\phi$  distribution. The acceptance for charged tracks is  
 86  $|\eta| < 0.9$  over the full azimuth. This hybrid technique combines two distinct track classes: (i) tracks  
 87 containing at least three hits (of up to six) in the ITS, including at least one hit in the SPD, and (ii) tracks  
 88 containing fewer than three hits in the ITS, or no hit in the SPD. The momentum of tracks of class (i)  
 89 is determined without a vertex constraint. The vertex constraint is however added for tracks of class (ii)  
 90 to improve the determination of their transverse momentum. The track momentum resolution  $\delta p_T/p_T$   
 91 is approximately 1% at  $p_T = 1 \text{ GeV}/c$  for all reconstructed tracks, and 4% at  $p_T = 40 \text{ GeV}/c$  for 95%  
 92 of all tracks. For tracks without a hit in the ITS (5% of the track sample) the resolution is 7% at  $p_T =$   
 93  $40 \text{ GeV}/c$ . The analysis is restricted to tracks with a Distance of Closest Approach (DCA) to the pri-  
 94 mary vertex smaller than 2.4 cm and 3.2 cm in the plane transverse to the beam and the beam direction,  
 95 respectively, in order to suppress contributions from secondary particles produced by weak decays and  
 96 interactions of primary particles with detector materials and beam pipe.

97 Tracks in the TPC are selected by requiring a  $p_T$  dependent minimum number of space points ranging  
 98 from 70 (of up to 159) for  $p_T = 0.15 \text{ GeV}/c$  to 100 at  $p_T > 20 \text{ GeV}/c$ . A  $\chi^2$  cut on the track fit is applied.  
 99 Secondary particles which are not produced at the primary vertex may acquire a wrong momentum when  
 100 constrained to the vertex. Therefore, a  $\chi^2$  cut on the difference between the parameters of the track fit  
 101 using all the space points in the ITS and TPC and using only the TPC space points with the primary vertex  
 102 position as an additional constraint is applied. The track reconstruction efficiency for primary charged  
 103 particles is approximately 60% at  $p_T = 0.15 \text{ GeV}/c$  and rises to a value of about 87% at  $1 \text{ GeV}/c$  and is  
 104 approximately uniform up to  $10 \text{ GeV}/c$  beyond which it decreases slightly. The efficiency is uniform in  
 105 azimuth and within the pseudorapidity range  $|\eta| < 0.9$ . Further details on the track selection procedure  
 106 and tracking performance can be found in [6].

## 107 **3 Jet reconstruction**

108 The charged jet reconstruction is carried out using the infrared-safe and collinear-safe sequential recom-  
 109 bination algorithms anti- $k_T$  [31] and  $k_T$  [32] from the FastJet package [33] and a seedless infrared safe  
 110 iterative cone based algorithm, named SIScone [34] to obtain the jet cross sections. The three jet finders  
 111 are found to be in good agreement within the uncertainties as discussed in Sec. 8.1. All other observables  
 112 (as discussed in Sec. 4) are analyzed with anti- $k_T$  only. Charged tracks with  $p_T > 0.15 \text{ GeV}/c$  and within  
 113  $|\eta| < 0.9$  are the inputs to the jet reconstruction algorithms. A boost invariant  $p_T$  recombination scheme

114 is used to determine the transverse momenta of jets by adding the charged particle transverse momenta.  
 115 Jets are reconstructed with resolution parameters  $R = 0.2, 0.3, 0.4,$  and  $0.6$  to enable a systematic study  
 116 of the production cross section and shape properties, as well as to provide a suite of references for mea-  
 117 surements performed in p–A and A–A collisions. The analyses reported in this work are restricted to  
 118 jets detected within the range  $|\eta| < (0.9 - R)$  in order to minimize edge effects in the reconstruction of  
 119 jets and biases on jet transverse profile and fragmentation functions. The inclusive jet cross sections are  
 120 reported as a function of  $p_T$  in the interval  $20 < p_T^{\text{jet, ch}} < 100$  GeV/c. The properties of the charged jet  
 121 with the highest  $p_T$  in the event, the so called *leading jet*, are presented in the same  $p_T$  interval.

## 122 4 Jet observables

123 The results are reported for a suite of charged jet properties including inclusive differential jet cross sec-  
 124 tion, charged particle multiplicity in leading jets ( $\langle N_{\text{ch}} \rangle$ ), leading jet size ( $\langle R_{80} \rangle$ ), radial distribution of  $p_T$   
 125 within the leading jet ( $\langle dp_T^{\text{sum}}/dr \rangle$ ), and jet fragmentation distributions ( $F^{p_T}, F^z, F^\xi$ ). The definition of  
 126 these observables and the methods used to measure them are presented in this section. Correction tech-  
 127 niques applied to measured raw distributions to account for instrumental effects (including the detector  
 128 acceptance and resolution), as well as the UE, are discussed in Sec. 6. All observables reported in this  
 129 work are corrected to particle level as defined in Sec. 5.

130 The differential jet cross section is evaluated using the following relation:

$$\frac{d^2\sigma^{\text{jet, ch}}}{dp_T d\eta}(p_T^{\text{jet, ch}}) = \frac{1}{\mathcal{L}^{\text{int}}} \frac{N_{\text{jets}}}{\Delta p_T \Delta \eta}(p_T^{\text{jet, ch}}), \quad (1)$$

131 where  $\mathcal{L}^{\text{int}}$  is the integrated luminosity,  $\Delta p_T$  and  $\Delta \eta$  are the selected  $p_T$  and  $\eta$  intervals. The number of  
 132 jets,  $N_{\text{jets}}$ , is measured for charged particle jets reconstructed with resolution parameter values,  $R = 0.2,$   
 133  $0.3, 0.4,$  and  $0.6,$  in the jet transverse momentum interval  $20 < p_T^{\text{jet, ch}} < 100$  GeV/c.

134 The charged particle multiplicity in leading jets,  $N_{\text{ch}}$ , is defined as the number of charged particles found  
 135 within the leading jet cone. Results for the mean charged particle multiplicity,  $\langle N_{\text{ch}} \rangle$ , computed in bins  
 136 of jet  $p_T$  are presented for resolution parameter values  $R = 0.2, 0.4,$  and  $0.6.$

137 The size of the leading jet,  $R_{80}$ , is defined as the radius in the  $\Delta \eta - \Delta \phi$  space that contains 80% of the  
 138 total  $p_T$  found in the jet cone. Results for the mean value,  $\langle R_{80} \rangle$ , are presented as a function of jet  $p_T$  for  
 139 resolution parameter values  $R = 0.2, 0.4,$  and  $0.6.$

140 The distribution of  $p_T$  density,  $dp_T^{\text{sum}}/dr$ , within a leading jet is measured as a function of the distance  
 141  $r = \sqrt{(\Delta \eta)^2 + (\Delta \phi)^2}$  from the jet direction. The momentum density is calculated jet by jet as a scalar  
 142 sum of the transverse momenta,  $p_T^{\text{sum}}$ , of all charged particles produced in annular regions of width  $\Delta r$   
 143 at radius  $r$  centered on the jet direction. The mean value of the momentum density,  $\langle dp_T^{\text{sum}}/dr \rangle$ , is evaluated  
 144 as a function of  $r$  using the following relation:

$$\left\langle \frac{dp_T^{\text{sum}}}{dr} \right\rangle(r) = \frac{1}{\Delta r} \frac{1}{N_{\text{jets}}} \sum_{i=1}^{N_{\text{jets}}} p_T^i(r - \Delta r/2, r + \Delta r/2) \quad (2)$$

145 where  $p_T^i(r - \Delta r/2, r + \Delta r/2)$  denotes the summed  $p_T$  of all tracks of jet  $i$ , inside the annular ring between  
 146  $r - \Delta r/2$  and  $r + \Delta r/2$ . The mean value is reported in bins of jet  $p_T$  for resolution parameter values  $R =$   
 147  $0.2, 0.4,$  and  $0.6.$   $N_{\text{jets}}$  denotes the number of jets per bin.

148 The fragmentation of the leading jet is reported based on the distributions

$$F^{p_T}(p_T, p_T^{\text{jet, ch}}) = \frac{1}{N_{\text{jets}}} \frac{dN}{dp_T}, \quad (3)$$

149

$$F^z(z^{\text{ch}}, p_T^{\text{jet, ch}}) = \frac{1}{N_{\text{jets}}} \frac{dN}{dz^{\text{ch}}}, \quad (4)$$

150

$$F^\xi(\xi^{\text{ch}}, p_T^{\text{jet, ch}}) = \frac{1}{N_{\text{jets}}} \frac{dN}{d\xi^{\text{ch}}}, \quad (5)$$

151 where  $N$  is the number of charged particles. The scaled  $p_T$  variables  $z^{\text{ch}} = p_T^{\text{particle}}/p_T^{\text{jet, ch}}$  and  $\xi^{\text{ch}} =$   
 152  $\log(1/z^{\text{ch}})$  are calculated jet by jet for each track. In contrast to the definition in [22], the energy carried  
 153 by neutral particles is not contained in the jet momentum. The (scaled)  $p_T$  spectra of the jet constituents  
 154 are normalized per jet and presented in bins of jet  $p_T$ .  $F^{p_T}$ ,  $F^z$  and  $F^\xi$  are complementary representations:  
 155 the particle  $p_T$  spectra  $F^{p_T}$  are less sensitive to uncertainties in the jet energy scale and may be more  
 156 suitable as a reference for future measurements in nuclear collisions than the standard representation  
 157  $F^z$ , whereas the  $F^\xi$  distributions emphasize fragmentation into low momentum constituents and are  
 158 particularly suited to demonstrate QCD coherence effects [35].

159 In this work, the averages  $\langle N_{\text{ch}} \rangle$ ,  $\langle R_{80} \rangle$ , and  $\langle dp_T^{\text{sum}}/dr \rangle$  are referred to as jet shape observables (jet  
 160 shapes) and  $F^{p_T}$ ,  $F^z$  and  $F^\xi$  as fragmentation distributions.

## 161 5 Monte Carlo simulations

162 Instrumental effects, such as the limited particle detection efficiency and the finite track momentum  
 163 resolution, induce momentum dependent particle losses and impact the jet energy scale and structures of  
 164 the observables reported in this work. The effect of the detector response is studied using the simulation  
 165 of the ALICE detector performance for particle detection and jet reconstruction. Simulated events are  
 166 generated with PYTHIA 6.425 [18] (tune Perugia-0 [36]) and the produced particles are transported with  
 167 GEANT3 [37]. The simulated and real data are analyzed with the same reconstruction algorithms. Jets  
 168 reconstructed based directly on the charged particle momenta produced by MC generators are hereafter  
 169 referred to as *particle level* jets whereas those obtained after processing the generator outputs through  
 170 GEANT and the ALICE reconstruction software are referred to as *detector level* jets. As the data are  
 171 corrected for instrumental effects, their comparison with simulation is done at particle level only.

172 The detector response to simulated charged jets with  $R = 0.4$  is illustrated in Fig. 1, showing on a jet-by-jet  
 173 basis the probability distribution of the relative difference between the charged jet  $p_T$  at the particle level  
 ( $p_T^{\text{jet, particle}}$ ) and at the detector level ( $p_T^{\text{jet, detector}}$ ). The probability distribution is shown for three different

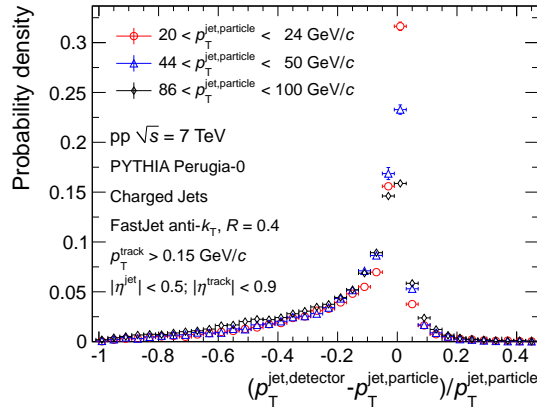


Fig. 1: (Color online) Probability distribution of the relative momentum difference of simulated ALICE detector response to charged jets in pp collisions at  $\sqrt{s} = 7$  TeV for three different  $p_T^{\text{jet, particle}}$  intervals. Charged jets are simulated using PYTHIA Perugia-0 and reconstructed with the anti- $k_T$  jet finding algorithm with  $R = 0.4$ .

174

175  $p_T^{\text{jet,particle}}$  intervals. The distributions have a pronounced maximum at zero ( $p_T^{\text{jet,detector}} = p_T^{\text{jet,particle}}$ ). The  
 176 tracking  $p_T$  resolution induces upward and downward fluctuations with equal probability, whereas the  
 177 finite detection efficiency of charged particles results in an asymmetric response. The probability that  
 178  $p_T^{\text{jet,detector}}$  is smaller than  $p_T^{\text{jet,particle}}$  varies between 88 and 92% as function of  $p_T^{\text{jet,particle}}$ .

179 The event generators PHOJET 1.12.1.35 [20], HERWIG 6.510 [19], and several PYTHIA tunes are used  
 180 for comparisons to data and for systematic investigations of the sensitivity of the MC correction factors to  
 181 variations of the detector response as well as to jet fragmentation and hadronization patterns. PYTHIA,  
 182 PHOJET, and HERWIG utilize different approaches to describe the parton shower and hadronization  
 183 process. HERWIG makes of angular ordering a direct part of the evolution process and thereby takes  
 184 correctly into account coherence effects in the emission of soft gluons. PYTHIA 6.4 is instead based on  
 185 transverse-momentum-ordered showers [38] in which angular ordering is imposed by an additional veto.  
 186 Phojet generates angular ordered initial-state radiation, whereas for final state radiation the mass-ordered  
 187 PYTHIA shower algorithm is used. Hadronization in PYTHIA and PHOJET proceeds via string break-  
 188 ing as described by the Lund model [39], whereas HERWIG uses cluster fragmentation. The PYTHIA  
 189 Perugia tune variations, beginning with the central tune Perugia-0 [36], are based on LEP, Tevatron, and  
 190 SPS data. The Perugia-2011 family of tunes [36] and the ATLAS Minimum Bias tune AMBT1 [40]  
 191 belong to the first generation of tunes that also use LHC pp data at  $\sqrt{s} = 0.9$  and 7 TeV with slight varia-  
 192 tions of the parameters controlling the modeling of the UE and fragmentation. Compared to the central  
 193 Perugia-2011 tune, AMBT1 uses a lower value of the infrared regularization scale for multiple partonic  
 194 interactions resulting in higher UE activity. It also uses a probability density of sum of two Gaussians  
 195 for the matter distribution inside the proton and a higher non-perturbative color-reconnection strength for  
 196 string fragmentation. The HERWIG generator version and PYTHIA tunes used in this work utilize the  
 197 CTEQ5L parton distributions [41], except for PYTHIA tune AMBT1 which uses MRST 2007LO\* [42].  
 198 PHOJET uses GRV94 [43].

## 199 6 Corrections

200 Two classes of correction techniques are used to account for instrumental effects in the measurements  
 201 reported in this work. The techniques are known as bin-by-bin correction and Bayesian unfolding [44].  
 202 A third technique based on Singular Value Decomposition (SVD) [45] is also used as a cross check.  
 203 The techniques and their comparative merits are presented in the following subsections. Corrections for  
 204 contamination from secondary particles and UE are discussed in Secs. 6.3 and 6.4 respectively.

205 The jet shapes and fragmentation distributions are corrected using the bin-by-bin method, while the  
 206 cross sections are corrected with the Bayesian unfolding technique. All observables are corrected for  
 207 secondaries contamination. All observables, except  $\langle R_{80} \rangle$ , are also corrected for UE contamination.

### 208 6.1 Bin-by-bin correction method

209 The bin-by-bin correction method is used to correct the jet shape observables and fragmentation func-  
 210 tions. To validate the method, it is also applied to the jet cross sections. It utilizes MC simulations as  
 211 described in Sec. 5 and is based on ratios of values for observables obtained at particle (generator) level  
 212 and detector level as a function of variable  $\mathbf{x}$ . In this work,  $\mathbf{x}$  can be 1-dimensional (e.g. jet  $p_T$  in case of  
 213 the jet spectra) or 2-dimensional (e.g. jet  $p_T$  and particle  $p_T$  in case of the fragmentation distributions).  
 214 Let  $O_{\text{mc}}^{\text{part}}(\mathbf{x})$  be the observable value at the particle level, and  $O_{\text{mc}}^{\text{det}}(\mathbf{x})$  the value obtained at the detector  
 215 level. The correction factors are defined as the ratio of the particle and detector level values of  $O_{\text{mc}}^{\text{part}}(\mathbf{x})$   
 216 and  $O_{\text{mc}}^{\text{det}}(\mathbf{x})$  in bins of  $\mathbf{x}$ . The corrected measurements,  $O_{\text{data}}^{\text{corrected}}$ , are obtained bin-by-bin by multiplying  
 217 the raw (uncorrected) values,  $O_{\text{data}}^{\text{uncorrected}}$ , as follows,

$$O_{\text{data}}^{\text{corrected}}(\mathbf{x}) = O_{\text{data}}^{\text{uncorrected}}(\mathbf{x}) \frac{O_{\text{mc}}^{\text{part}}(\mathbf{x})}{O_{\text{mc}}^{\text{det}}(\mathbf{x})}. \quad (6)$$

218 The correction factors depend on the shape of the simulated jet spectrum and fragmentation distributions.  
 219 Systematic uncertainties related to the accuracy with which data are reproduced by the simulations are  
 220 discussed in Sec. 7.2.

221 Correction factors obtained for the jet  $p_T$  spectra range from 25% to 50% and reach a maximum at  
 222 100 GeV/c. The bin-by-bin corrections applied to jet shape observables include subtraction of contam-  
 223 ination associated with the production of secondary particles within the detector. Correction factors  
 224 obtained for  $\langle N_{\text{ch}} \rangle$  at  $R = 0.2$  (0.4, 0.6) are of the order of 2-6% (3-5%, 4-6%) while for  $\langle R_{80} \rangle$  at  $R = 0.2$   
 225 (0.4, 0.6) they are found in the range 5-7% (2-10%, 4-9%). Correction factors applied on radial mo-  
 226 mentum densities have a maximum value of 12% (15%, 19%) at  $R = 0.2$  (0.4, 0.6). In contrast, for the  
 227 fragmentation distributions, the bin-by-bin correction and the correction for the contamination from sec-  
 228 ondaries, discussed in Sec. 6.3, are carried out in separate steps. The typical value of the corrections at  
 229 the maximum of the  $F^\xi$  distribution is of the order of few percent only. The correction factors for  $F^{p_T}$   
 230 and  $F^z$  are largest at low particle  $p_T$  (up to 50%), where the tracking efficiency is smallest, and at the  
 231 highest  $z^{\text{ch}}$  (up to 40%) where the impact of the track momentum resolution is strong and detector effects  
 232 at the track level strongly influence the reconstructed jet momentum.

## 233 6.2 Unfolding using response matrix inversion techniques

234 Instrumental effects associated with acceptance, particle losses due to limited efficiency, and finite mo-  
 235 mentum resolution are modeled using a detection response matrix, which is used to correct observ-  
 236 ables for these effects. The jet  $p_T$  response matrix is determined by processing MC events through  
 237 a full ALICE detector simulation as described in Sec. 5. The particle level (true),  $T(t)$ , and detector  
 238 level (measured),  $M(m)$ ,  $p_T$  spectra of the leading jet are both subdivided in 11 bins in the interval  
 239  $20 < p_T^{\text{jet, ch}} < 100$  GeV/c. The matrix elements  $R_{mt}$  express the conditional probability of measuring  
 240 a jet  $p_T$  in bin,  $m$  given a true value in bin,  $t$ . The measured distribution,  $M$ , can thus be estimated by  
 241 multiplying the true distribution,  $T$ , by the response matrix,

$$M = RT. \quad (7)$$

242 Experimentally, the unfolding problem involves the determination of  $T$  given  $M$ . This is symbolically  
 243 written as

$$T = R^{-1}M. \quad (8)$$

244 However the matrix  $R$  may be singular and can not always be inverted analytically. Consequently, other  
 245 numerical techniques are needed to obtain the true, physically meaningful, distribution  $T$  given a mea-  
 246 sured distribution  $M$ . Furthermore, the exact solution, even if it exists, is usually unstable against small  
 247 variations in the initial estimates of the measured distribution, and oscillating due to finite statistics in the  
 248 measured distribution. This problem can be overcome using a regularization condition based on a priori  
 249 information about the solution.

250 The Bayesian unfolding technique [44] is an iterative method based on Bayes' theorem. Given an initial  
 251 hypothesis (a prior),  $P_t$ , with  $t = 1, \dots, n$ , for the true momentum and reconstruction efficiency,  $\varepsilon_t$ , Bayes'  
 252 theorem provides an estimator of the inverse response matrix elements,  $\tilde{R}_{tm}$ ,

$$\tilde{R}_{tm} = \frac{R_{mt}P_t}{\varepsilon_t \sum_{t'} R_{mt'}P_{t'}}. \quad (9)$$

253 The measured distribution,  $M_m$ , is thus unfolded as follows

$$P'_t = \sum_m \tilde{R}_{tm} M_m, \quad (10)$$

254 to obtain a posterior estimator,  $P'_t$ , of the true distribution. The inversion is improved iteratively by  
 255 recursively using posterior estimators to update and recalculate the inversion matrix. The number of

256 iterations serves as a regularization parameter in the unfolding procedure. For jet spectra studies, the  
 257 measured spectra are used as prior and convergence is obtained typically after three iterations.

258 As an additional cross check, the analysis of charged jet cross sections is also carried out with the RooUn-  
 259 fold implementation of the Singular Value Decomposition (SVD) unfolding technique [45, 46] using  
 260 raw measured spectra as prior distributions. The performance of the Bayesian unfolding, SVD unfold-  
 261 ing, and bin-by-bin correction methods are compared based on PYTHIA Perugia-0 simulated jets. The  
 262 three methods produce results that are found to be within 4% of the truth distribution. The cross sections  
 263 reported in this work are obtained with the Bayesian unfolding method.

### 264 **6.3 Contamination from secondary particles**

265 Charged secondary particles are predominantly produced by weak decays of strange particles (e.g.  $K_S^0$   
 266 and  $\Lambda$ ), decays of charged pions, conversions of photons from neutral pion decays and hadronic inter-  
 267 actions in the detector material. The charged jet transverse momentum, jet shapes and fragmentation  
 268 distributions include by definition only primary charged jet constituents. Secondary particles introduce  
 269 ambiguities in the jet energy scale and contribute to the raw reconstructed multiplicity, momentum den-  
 270 sity, and fragmentation distributions. Although their contribution is minimized by the analysis cuts de-  
 271 scribed in Sec. 2, the measured distributions nonetheless must be corrected for a small residual contam-  
 272 ination. The subtraction of the secondary particle contamination is implicitly included in the bin-by-bin  
 273 correction applied for measurements of jet shape observables. It is however carried out separately and  
 274 explicitly in the measurements of the fragmentation function. The contribution of secondaries is esti-  
 275 mated from MC simulations, separately for each bin in jet  $p_T$  and particle  $p_T$ ,  $z^{\text{ch}}$  and  $\xi^{\text{ch}}$ . The correction  
 276 applied to the measured fragmentation functions is highest, up to 35%, at small  $p_T$  and large  $\xi^{\text{ch}}$ . It  
 277 amounts to few percent only when averaged over all jet constituents. To enhance the low strangeness  
 278 yield in the PYTHIA Perugia-0 simulations to the level observed in data, the contamination estimate is  
 279 multiplied by a data-driven correction factor based on measurements [47] of strange particle production  
 280 in non-single-diffractive events by the CMS collaboration and simulations from [48]. The contamination  
 281 of secondaries from strange particle decays is small, and the effect of the strangeness scaling on the  
 282 final result is less than 1%. No scaling is applied on the correction to the jet spectrum and jet shape  
 283 observables.

### 284 **6.4 Underlying event subtraction**

285 There is no strict definition of the Underlying Event. Operationally, it corresponds to all particles pro-  
 286 duced in an event that are not an integral part of a jet or produced directly by hard scattering of partons.  
 287 The ATLAS [49, 50], CMS [51] and ALICE [52] collaborations have already published studies of UE  
 288 in pp collisions at  $\sqrt{s} = 7$  TeV. In this work, a similar method is adopted to determine the UE yield and  
 289 correct the measured jet observables for this source of contamination.

290 The UE particle yield is estimated event-by-event based on circular regions perpendicular to the measured  
 291 jet cones as in [14]. The circular regions have the same size as the jet resolution parameter and are placed  
 292 at the same pseudorapidity as the leading jet but offset at an azimuthal angle  $\Delta\phi = \pi/2$  relative to the jet  
 293 axis.

294 For the jet cross section measurements, the UE is subtracted on a jet-by-jet basis prior to unfolding and  
 295 the same treatment is applied to jets obtained from simulations before jet response matrix is created.

296 In the case of the fragmentation and jet shape observables, no correction for the UE contribution to the  
 297 reconstructed jet energy is applied, but the UE contribution to the measured distributions in each bin of  
 298 jet  $p_T$  is subtracted. The  $p_T$  spectra of particles in the perpendicular cone are accumulated and averaged  
 299 over many events. To account for variations of the cone size of the anti- $k_T$  jets, the spectra are weighted  
 300 jet by jet with the ratio of the cone size, determined by FastJet, to the nominal aperture of  $\pi R^2$  for a jet



301 with resolution parameter  $R$ . The difference between the weighted and unweighted UE distributions is at  
 302 the level of 1%. The  $\xi^{\text{ch}}$  variable is computed jet-by-jet for each particle using the transverse momentum  
 303 of the leading jet. The radial  $p_{\text{T}}$  sum distributions are obtained relative to the axis of the perpendicular  
 304 cone.

305 The algorithms used for jet reconstruction are sensitive to statistical fluctuations of the particle density  
 306 which are possibly enhanced by local variations of the detection efficiency and secondary particle pro-  
 307 duction. This reconstruction bias may differ for the jet region and the UE region. Hence, the UE distri-  
 308 butions are corrected first for tracking efficiency, resolution and contamination from secondary particles.  
 309 The fully corrected distributions are then subtracted in bins of the leading jet transverse momentum.  
 310 The correction is smaller than 2.5% of the charged jet energy, but it is considerable for the fragmen-  
 311 tation distributions at the lowest track momentum and highest  $\xi^{\text{ch}}$ , where the ratio of UE background  
 312 to fragmentation signal takes values up to 2.5. No self-consistent technique exists to subtract the UE  
 313 in the  $\langle R_{80} \rangle$  measurements, these measurements are therefore reported without correction for UE con-  
 314 tamination. However, comparing the radial  $\langle dp_{\text{T}}^{\text{sum}}/dr \rangle$  distributions before and after UE subtraction, the  
 315 increase in jet size  $\langle R_{80} \rangle$  due to the UE is estimated to be of the order of few percent only. The systematic  
 316 uncertainties for not performing the UE subtraction are thus found negligible compared to other sources  
 317 of errors in the measurements of  $\langle R_{80} \rangle$ .

## 318 7 Estimation of systematic uncertainties

319 A summary of all systematic uncertainties for selected bins is given in Table 1 for the cross section  
 320 measurements, and in Table 2 for the  $\langle N_{\text{ch}} \rangle$ ,  $\langle R_{80} \rangle$ ,  $\langle dp_{\text{T}}^{\text{sum}}/dr \rangle$ ,  $F^{p_{\text{T}}}$ ,  $F^{p_{\text{T}}}$  and  $F^z$  distributions. The  
 321 uncertainties given in each column of the table are described in this section.

### 322 7.1 Tracking efficiency and resolution

323 Uncertainties associated with the momentum resolution and charged track reconstruction efficiency lead  
 324 to systematic uncertainties in measurements of the jet cross section, jet shapes, and jet fragmentation  
 325 functions.

326 The systematic uncertainty on tracking efficiency is estimated to be 5% based on several variations of  
 327 cuts used in the track selection introduced earlier. The uncertainty on the track momentum resolution  
 328 amounts to 20% [53].

329 In order to evaluate the effect of these uncertainties on the measured jet cross sections, the corresponding  
 330 rescaled response matrix is used to unfold the spectra. For the jet shape and fragmentation observables,  
 331 the impact of the finite detector efficiency and momentum resolution on the bin-by-bin correction factors  
 332 is estimated by applying parametrized detector response to PYTHIA events clustered with FastJet, and  
 333 varying the efficiency and resolution independently. Systematic uncertainties for the jet particle mul-  
 334 tiplicity and jet shape observables are given in Table 2 for a resolution parameter  $R = 0.4$ . For larger  
 335 (smaller)  $R$ , a moderate increase (decrease) of the uncertainties is observed related to tracking efficiency.  
 336 For the fragmentation distributions, variations of the momentum resolution induce the most significant  
 337 changes at high track  $p_{\text{T}}$ . The systematic uncertainties due to the efficiency variations are largest at the  
 338 highest  $z^{\text{ch}}$  and smallest at intermediate values.

### 339 7.2 Bin-by-bin correction

340 The data correction methods used in this work are largely based on tune Perugia-0 of the PYTHIA event  
 341 generator. The particular structure of jets produced by PYTHIA might however conceivably affect the  
 342 magnitude, and dependencies of the correction factors on the jet momentum, particle momentum, or ra-  
 343 dial dependence  $r$ . The possible impact of such event generator dependencies is examined by comparing  
 344 the amplitude of the bin-by-bin corrections obtained with PYTHIA tunes Perugia-0 and Perugia-2011,

345 with those obtained with the HERWIG generator. This is accomplished with a parametrized detector  
 346 response and the anti- $k_T$  jet finder. In addition, the impact of modifications of the jet fragmentation is  
 347 studied by artificially duplicating and removing jet particles with a momentum dependent probability.  
 348 The variations are constrained to be at a similar level as the differences observed between simulations  
 349 and data reaching up to a factor of 2.5 for values of  $z^{\text{ch}}$  close to 1 in the fragmentation distributions. The  
 350 charged particle multiplicity is affected by  $\sim 30\%$ . The resulting systematic uncertainties are largest for  
 351 high values of  $z^{\text{ch}}$  and track  $p_T$  and small values of  $\xi^{\text{ch}}$ .

352 As an independent check, a closure test with a 2-dimensional folding technique is carried out on the  
 353 fragmentation distributions from an inclusive jet sample (comprising leading and sub-leading jets). A  
 354 response matrix in bins of generated and reconstructed jet  $p_T$  and particle (scaled) transverse momentum  
 355 is used to fold the corrected results back to the uncorrected level. Since the folding method has negligible  
 356 dependence on the event generator, the comparison of the folded to the original distributions reveals  
 357 possible biases of the bin-by-bin correction. The observed non-closure at the level of few percent is  
 358 consistent with the systematic uncertainty assigned to the bin-by-bin correction from modifications of  
 359 the fragmentation pattern.

### 360 7.3 Response unfolding

361 The unfolding techniques used in this work correct the measured jet spectra for the detector response.  
 362 The limited measurement resolution, discussed in Sec. 5, results in a small, but finite, probability for  
 363 bin migration of the reconstructed jet momentum relative to the true value. Consequently, the unfolding  
 364 introduces a correlation between neighbouring bins of the corrected spectrum, and statistical fluctuations  
 365 in the measured data result in a spectral shape systematic uncertainty. To assess this uncertainty, the  
 366 raw jet spectra are smeared by a Gaussian function with a width given by the statistical uncertainty in the  
 367 given momentum bin. The resulting spectra are then unfolded and the systematic uncertainty is evaluated  
 368 as a spread of the corrected spectra. The value of this systematic uncertainty increases roughly linearly  
 369 with  $p_T^{\text{jet, ch}}$ , reaching a maximum value of  $\sim 7\%$  at  $p_T^{\text{jet, ch}} \approx 100 \text{ GeV}/c$ .

### 370 7.4 Underlying event subtraction

371 In this work, we use perpendicular cones to measure and subtract the UE as described in Sec. 6.4. How-  
 372 ever, there is no unique prescription on how to determine the UE. In a prior, trigger hadron based, UE  
 373 analysis by the ALICE collaboration [52], a geometrically different definition of the transverse region  
 374 was used. The charged particle transverse momentum densities obtained in our analysis are consistent  
 375 with the saturation values in the transverse region measured in [52]. In [55], the UE was estimated from  
 376 dijet events and imposing an additional veto on a third jet. An alternative simulation to estimate and sub-  
 377 tract the UE in a similar way is performed using particle level output from a MC event generator. The UE  
 378 is measured from events with a dijet in the detector acceptance, to understand if and how the non-leading  
 379 jet affects the UE estimate, rejecting events with additional charged jets with a  $p_T$  exceeding  $8 \text{ GeV}/c$ .  
 380 The resulting difference on the fragmentation distributions is used to assign a 5% systematic uncertainty  
 381 to the estimated UE. The resulting systematic uncertainty on the fragmentation distributions is highest  
 382 at low transverse momenta. Systematic uncertainties on  $\langle dp_T^{\text{sum}}/dr \rangle$  are largest at large distances  $r$  in the  
 383 jet  $p_T$  interval 20 - 30  $\text{GeV}/c$ . The uncertainty increases for higher values of the resolution parameter  $R$ .  
 384 Systematic uncertainties on the measured charged jet cross sections are smaller than 1% and considered  
 385 negligible.

386 The anti- $k_T$  jet finder typically produces circular jet cones, and the UE contribution to the jet shapes and  
 387 fragmentation distributions is evaluated consistently in circular cones. In individual jets, particles may  
 388 however be added at a distance  $r \geq R$  thereby giving rise to a convex deformation of the cone. Concave  
 389 deformations might also occur. The dependence of the fragmentation distributions on the cone shape is  
 390 checked by repeating the analysis using only tracks in an ideal cone around the jet axis. In this case no

jet area scaling of the UE is applied. The low momentum particle yield is most affected: at high jet radii, low  $z^{\text{ch}}$  fragmentation dominates over high  $z^{\text{ch}}$  fragmentation. In addition, the probability to collect a soft particle from the UE is comparatively higher than at small  $r$ . The observed effect is negligibly small: a maximum depletion of 4% of the particle yield at the highest  $\xi^{\text{ch}}$  in the smallest jet momentum bin is observed. Considerably smaller variations are found for all other jet momenta and  $\xi^{\text{ch}}$  bins. The effect is reproduced in MC simulations, and no systematic uncertainty is associated to the jet cone shape.

### 7.5 Cross section normalization

The determination of luminosity and related systematic uncertainties are discussed in [54]. A normalization uncertainty of 3.5% is assigned to the cross section measurement.

### 7.6 Contamination from secondary particles

The reconstructed primary particles originate from the main interaction vertex and have a non-zero distance of closest approach DCA because of finite resolution effects. The DCA of secondaries however spans a much broader range of values. Reducing the maximum allowed DCA value reduces contaminations from secondaries but also reduces the detection efficiency of primary particles. In this analysis, primary particles are selected requiring a small DCA as discussed in Sec. 2, and a correction for the residual contribution of secondary particles is applied, as explained in Sec. 6.3. The systematic uncertainty associated to the correction is estimated by reducing the maximum allowed DCA used in the selection of primary tracks by more than a factor of 9 using a  $p_{\text{T}}$  dependent cut. The resulting fragmentation distributions are corrected consistently for contamination and cut efficiency and residual differences in the fully corrected spectra are assigned as systematic uncertainty. The highest uncertainty is found for large values of  $\xi^{\text{ch}}$ .

The dependence of the correction on the strange particle yield in the PYTHIA Perugia-0 simulations is estimated from comparison to data as explained in Sec. 6.3. The effect on the jet cross sections is less than 3% and is assigned as systematic uncertainty. For the jet shape observables it is negligible.

Table 1: Summary of systematic uncertainties for selected bins in selected cross section distributions

Distribution	Bin (GeV/c)	Track eff. (%)	Track $p_{\text{T}}$ res. (%)	Unfolding (%)	Normalization (%)	Sec. (%)	Total (%)
$\frac{d^2\sigma^{\text{jet, ch}}}{dp_{\text{T}}d\eta}$ ( $R = 0.2$ )	20-24	+4.6 -4.2	4.0	3.0	3.5	1.9	+7.8 -7.6
	50-58	+22.1 -10.5	4.0	1.6	3.5	2.5	+23.0 -12.2
	86-100	+26.0 -15.3	4.0	5.2	3.5	2.8	+27.1 -17.2
$\frac{d^2\sigma^{\text{jet, ch}}}{dp_{\text{T}}d\eta}$ ( $R = 0.4$ )	20-24	+7.5 -4.5	4.0	3.0	3.5	2.1	+9.9 -7.9
	50-58	+23.2 -10.6	4.0	1.4	3.5	2.5	+24.0 -12.2
	86-100	+24.9 -15.0	4.0	5.6	3.5	2.7	+26.2 -17.2
$\frac{d^2\sigma^{\text{jet, ch}}}{dp_{\text{T}}d\eta}$ ( $R = 0.6$ )	20-24	+11.1 -5.3	4.0	6.6	3.5	2.3	+14.2 -10.3
	50-58	+22.6 -14.3	4.0	1.9	3.5	2.6	+23.4 -15.6
	86-100	+23.7 -13.7	4.0	6.0	3.5	2.7	+25.1 -16.1

Table 2: Summary of systematic uncertainties for selected bins in selected jet shape and fragmentation distributions for  $R = 0.4$ .

Distribution	Bin	Track eff. (%)	Track $p_T$ res. (%)	Bin-by-bin corr. (%)	UE (%)	Sec. (%)	Total (%)
$\langle N_{\text{ch}} \rangle$	20-25 GeV/c	+5.8 -5.1	+4.0 -3.5	+0.7 -0.9	0.8	negligible	+7.1 -6.2
	80-100 GeV/c	+5.8 -5.1	+4.0 -3.5	+0.7 -0.9	0.5	negligible	+7.1 -6.2
$\langle R_{80} \rangle$	20-25 GeV/c	+6.1 -5.5	+3.6 -4.3	+1.7 -1.7	—	—	+7.2 -7.2
	80-100 GeV/c	+6.1 -5.5	+3.6 -4.3	+1.7 -1.7	—	—	+7.2 -7.2
$\langle \frac{dp_T^{\text{sum}}}{dr} \rangle$ $20 < p_T^{\text{jet, ch}} < 30$ GeV/c	0.00 - 0.04	+8.1 -6.5	+5.9 -2.4	+2.9 -3.1	negligible	negligible	+10.5 -7.6
	0.20 - 0.24	+8.1 -6.5	+5.9 -2.4	+2.9 -3.1	0.3	negligible	+10.5 -7.6
	0.36 - 0.40	+8.1 -12.0	+5.9 -2.4	+2.9 -3.1	15.0	negligible	+18.3 -19.6
$\langle \frac{dp_T^{\text{sum}}}{dr} \rangle$ $60 < p_T^{\text{jet, ch}} < 80$ GeV/c	0.00 - 0.04	+10.6 -5.1	+5.6 -6.5	+3.7 -3.4	negligible	negligible	+12.6 -8.9
	0.20 - 0.24	+10.6 -5.1	+5.6 -6.5	+3.7 -3.4	0.4	negligible	+12.7 -9.0
	0.36 - 0.40	+10.6 -5.1	+5.6 -6.5	+3.7 -3.4	1.6	negligible	+12.7 -9.1
$F_{p_T}$ $20 < p_T^{\text{jet, ch}} < 30$ GeV/c	0 - 1 GeV/c	5.0	0.1	0.7	3.3	3.2	6.8
	6 - 7 GeV/c	0.8	negligible	2.3	negligible	0.5	2.4
	18 - 20 GeV/c	9.9	0.5	6.0	negligible	0.4	11.6
$F_{p_T}$ $60 < p_T^{\text{jet, ch}} < 80$ GeV/c	0 - 5 GeV/c	5.2	0.3	0.2	0.8	2.1	5.7
	20 - 30 GeV/c	1.4	negligible	3.7	negligible	0.6	4.0
	50 - 60 GeV/c	10.5	3.5	9.6	negligible	0.6	14.6
$F^z$ $20 < p_T^{\text{jet, ch}} < 30$ GeV/c	0 - 0.1	4.7	1.6	0.2	1.6	1.4	5.2
	0.3 - 0.4	0.4	negligible	2.7	negligible	0.3	2.8
	0.9 - 1.0	15.5	1.1	4.8	negligible	0.6	16.3
$F^z$ $60 < p_T^{\text{jet, ch}} < 80$ GeV/c	0 - 0.1	5.0	0.3	0.3	0.7	1.3	5.3
	0.3 - 0.4	1.2	0.2	3.7	negligible	0.4	3.9
	0.8 - 1.0	13.8	3.1	6.1	negligible	1.2	15.4
$F^\xi$ $20 < p_T^{\text{jet, ch}} < 30$ GeV/c	0 - 0.4	9.9	0.5	4.6	negligible	0.7	10.9
	0.8 - 1.2	0.6	negligible	3.0	negligible	0.5	3.1
	4.8 - 5.3	5.1	0.7	0.9	15.3	7.8	17.9
$F^\xi$ $60 < p_T^{\text{jet, ch}} < 80$ GeV/c	0 - 1.0	5.0	0.5	3.9	negligible	0.7	6.4
	1.0 - 2.0	1.3	0.4	3.4	negligible	0.6	3.8
	5.0 - 6.2	5.7	0.2	0.7	6.5	6.2	10.6

## 415 8 Results

### 416 8.1 Comparison of jet finding algorithms

417 Figure 2 (top panel) shows the differential cross sections of charged jet production measured in pp collisions at  $\sqrt{s} = 7$  TeV using the  $k_T$ , anti- $k_T$ , and SIS Cone jet finding algorithms. The distributions are

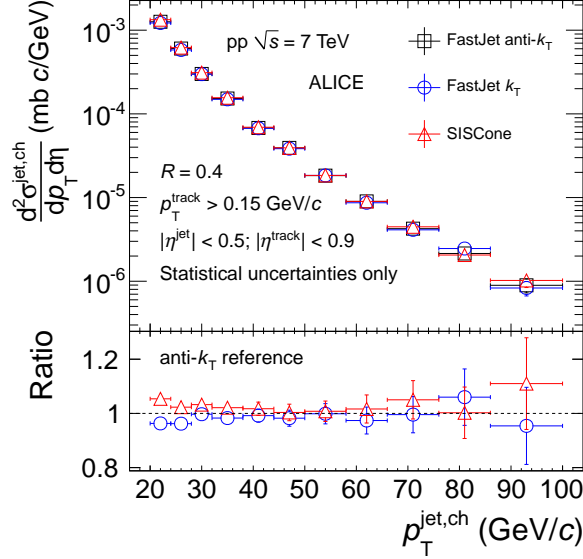


Fig. 2: (Color online) Top panel: Charged jet cross sections in pp collisions at  $\sqrt{s} = 7$  TeV. Symbols correspond to different algorithms used for jet reconstruction. Bottom panel: Ratios between jet cross sections obtained by  $k_T$ , and SIS Cone to that obtained by anti- $k_T$ .

418 obtained with a resolution parameter,  $R = 0.4$ , for jets in the pseudorapidity range  $|\eta^{\text{jet}}| < 0.5$ , and  
 419 transverse momenta from 20 to 100 GeV/c. The bottom panel of the figure displays the ratios between  
 420 the cross sections obtained with the  $k_T$ , and SIS Cone algorithms to those obtained with the anti- $k_T$  as  
 421 a function of the jet transverse momentum. For a correct treatment of statistical correlations between the  
 422 numerator and denominator, the data were divided into fully correlated and uncorrelated subsets. The  
 423 distributions are corrected using the bin-by-bin correction procedure described in Sec. 6.1. The ratios  
 424 of the jet cross sections are consistent with unity over nearly the entire range of jet transverse momenta  
 425 spanned by this analysis. A significant deviation of 5% is observed only in the lowest  $p_T$  bin ( $p_T^{\text{jet, ch}} = 20$ -  
 426 24 GeV/c) between the SIS Cone and anti- $k_T$  algorithms. For larger  $p_T^{\text{jet, ch}}$  SIS Cone and  $k_T$  algorithms  
 427 agree within errors with the anti- $k_T$  algorithm.  
 428

429 The anti- $k_T$  algorithm initiates particle clustering around the highest  $p_T$  particles of an event. In contrast,  
 430 the  $k_T$  algorithm initiates jet finding by clustering particles with the lowest momenta. It is thus rather  
 431 sensitive to events with a large, fluctuating density of low momentum particles as produced in A–A  
 432 collisions. The anti- $k_T$  algorithm does not exhibit such sensitivity and is thus favored for studies of jet  
 433 production in A–A collisions. Since there are no large differences observed between the spectra obtained  
 434 with the three jet finders discussed above, and considering the fact that the results of this work will be  
 435 used as a reference for similar measurements in A–A and p–A collisions, the remainder of the analyses  
 436 presented in this work are performed with the anti- $k_T$  algorithm exclusively.

### 437 8.2 Charged jet cross section

438 Figure 3 presents the fully corrected inclusive charged jet cross section measured in pp collisions at  
 439  $\sqrt{s} = 7$  TeV using the anti- $k_T$  jet finder. Corrections for the detector response and instrumental effects  
 440 are carried out using the Bayesian unfolding method presented in Sec. 6.2. The distributions are also cor-

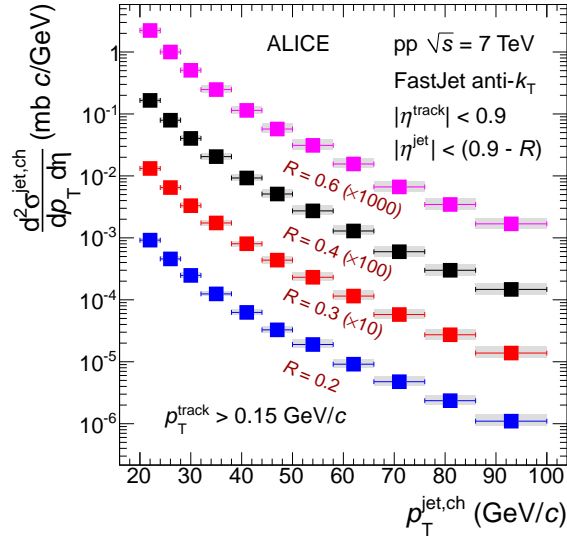


Fig. 3: (Color online) Inclusive charged jet cross sections in pp collisions at  $\sqrt{s} = 7$  TeV using the anti- $k_T$  algorithm with  $R = 0.2$  ( $0.3$ ,  $0.4$ , and  $0.6$ ) within  $|\eta^{\text{jet}}| \leq 0.7$  ( $|\eta^{\text{jet}}| \leq 0.6$ ,  $|\eta^{\text{jet}}| \leq 0.5$ , and  $|\eta^{\text{jet}}| \leq 0.3$ ).

441 rected for UE contamination on an event-by-event basis according to the method described in Sec. 6.4.  
 442 Inclusive charged jet cross sections are reported for resolution parameter values  $R = 0.2$ ,  $0.3$ ,  $0.4$  and  $0.6$ ,  
 443 and limited to pseudorapidity ranges  $|\eta| < (0.9 - R)$  in order to avoid losses due to partially reconstructed  
 444 jets at the edge of the pseudorapidity acceptance. Statistical uncertainties are displayed as vertical error  
 445 bars. Individual sources of systematic uncertainties are  $p_T$  dependent. In Fig. 3 as well as in all other  
 446 figures the data points are placed at the bin centre along the abscissa and the horizontal error bars indicate  
 447 the bin width while the vertical error bars indicate the statistical uncertainties. The total systematic un-  
 448 certainties are obtained as a quadratic sum of individual systematic uncertainties, as described in Sec. 7,  
 449 and are shown as shaded bands around the data points in Fig. 3 as well as in all other figures.

450 The measured charged jet cross sections are compared to those reported by the ATLAS experiment [3] at  
 451  $R = 0.4$  and  $0.6$  in Fig. 4. The ATLAS charged jets are measured in the rapidity  $|y| \leq 0.5$  at both  $R = 0.4$   
 452 and  $0.6$ , using charged tracks with  $p_T \geq 0.3$  GeV/c without underlying event subtraction. The ALICE  
 453 therefore also uses the same track  $p_T$  selection without underlying event subtraction unlike Fig. 3. To  
 454 quantify the level of agreement between the ALICE and ATLAS jet cross section measurements, the  
 455 ALICE data are fitted with a modified Tsallis [56] distribution ( $f(p_T) = a \cdot (1 + \frac{p_T}{b})^{-c}$ ). The Tsallis fits  
 456 are shown as dotted black curves in the top panels of Fig. 4. The  $\chi^2/dof$  of the fits are  $2.97/8$  and  
 457  $4.27/8$  for  $R = 0.4$  and  $0.6$  respectively. The bottom panels of Fig. 4 show the ratios of the ALICE and  
 458 ATLAS data points to the fit function. The gray bands represent the systematic uncertainties on ALICE  
 459 data points. Despite fluctuations in the high  $p_T$  range of the ATLAS data, both datasets are in excellent  
 460 agreement.

461 In the top panels of Fig. 5, the measured charged jet cross sections are compared to predictions from  
 462 PYTHIA (tunes Perugia-0, Perugia-2011, and AMBT1), PHOJET, and HERWIG for  $R = 0.2$ ,  $0.4$  and  
 463  $0.6$ . The ratios of the MC simulations to measured data are shown in the bottom panels of Fig. 5. In  
 464 the high  $p_T$  range, PYTHIA Perugia-2011 describes the data best, while in the low  $p_T$  range data is best  
 465 described by HERWIG and PHOJET. All PYTHIA tunes systematically overestimate the measured data  
 466 in the low transverse momentum range and the discrepancy increases with increasing cone size. The  
 467 worst discrepancy with the data is observed for the PYTHIA tune AMBT1, which overestimates the data  
 468 by factors ranging from 25% to 75% over the studied  $p_T$  range for  $R = 0.2$ . The disagreement grows with  
 469 increasing resolution parameter, and is worst for  $R = 0.6$ .

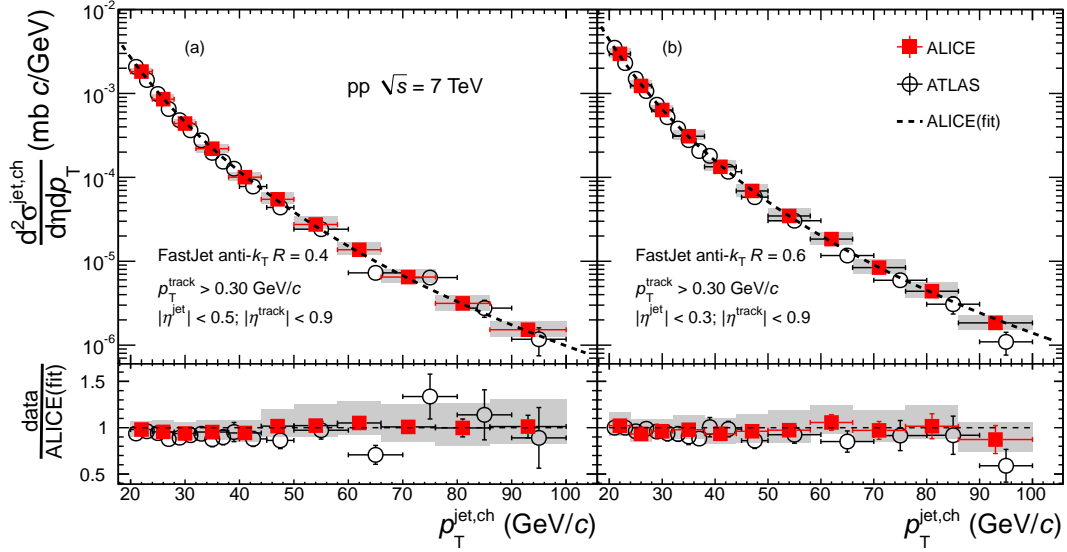


Fig. 4: (Color online) Top panels: Comparison of the charged jet cross section in the ALICE and the ATLAS [3] experiments in pp collisions at  $\sqrt{s} = 7$  TeV. Statistical and systematic uncertainties are shown separately for ALICE data points, the gray bands indicating the systematic uncertainties, while for the ATLAS data points, the error bars show the statistical and systematic uncertainties summed in quadrature. The dotted line represents a Tsallis fit used to parametrize the ALICE data. Bottom panels: The ratio of the ALICE and ATLAS charged jet spectrum to the parametrized ALICE data. Note that the labels in the figures correspond to the ALICE measurements (see text for details).

470 Figure 6 shows the ratios of cross sections for jets with resolution parameters  $R = 0.2$ ,  $R = 0.4$  and  
 471  $R = 0.2$ ,  $R = 0.6$ . The ratio of jet spectra [6] is sensitive to the collimation of particles around the  
 472 jet axis and serves as an indirect measure of the jet structure used particularly in A–A collisions [57],  
 473 where large background fluctuations greatly complicate jet shape studies. In order to compare the ratios  
 474 within the same jet pseudorapidity range, the ratios are studied within  $|\eta| < 0.3$ , which coincides with  
 475 the fiducial jet acceptance for the largest resolution parameter studied ( $R = 0.6$ ). To avoid statistical  
 476 correlations between the numerator and denominator, disjoint subsets of the data are used. The measured  
 477 ratios are also compared to those from PYTHIA Perugia-2011 and HERWIG simulations. The measured  
 478 ratios confirm the expected trend of increased collimation with increasing transverse momentum of jets,  
 479 corroborated also by the simulation results. At high  $p_T$  ( $> 30$  GeV/c), both PYTHIA and HERWIG are  
 480 in good agreement with the data within uncertainties. However at low  $p_T$  ( $< 30$  GeV/c) PYTHIA tends  
 481 to underpredict the data for both the ratios whereas HERWIG tends to overpredict the data for the ratio  
 482  $\sigma^{\text{jet, ch}}(R = 0.2) / \sigma^{\text{jet, ch}}(R = 0.6)$ .

### 483 8.3 Charged particle multiplicity in the leading jet

484 The corrected mean charged particle multiplicity distributions  $\langle N_{\text{ch}} \rangle$  in the leading jet are shown in Fig. 7  
 485 (left panel) as a function of jet  $p_T$  for  $R = 0.2$ ,  $0.4$ , and  $0.6$ . The  $\langle N_{\text{ch}} \rangle$  rises monotonically with increasing  
 486 jet  $p_T$  as well as with increasing  $R$ . These results are in qualitative agreement with those reported by the  
 487 CDF [8] collaboration and more recently by the CMS [12] collaboration based on slightly different  
 488 kinematic track cuts.

489 In the left panel of Fig. 7, the measurements are compared to predictions by the MC models PYTHIA  
 490 (tunes Perugia-0, Perugia-2011, AMBT1), PHOJET, and HERWIG. Ratios of the predictions to the data  
 491 are displayed in the right panel. The model predictions are well within 10% of the measured data with  
 492 largest deviations of  $\sim 15\%$  at  $R = 0.6$  and  $0.2$  towards large jet  $p_T$ . The PYTHIA tune Perugia-0 tends to

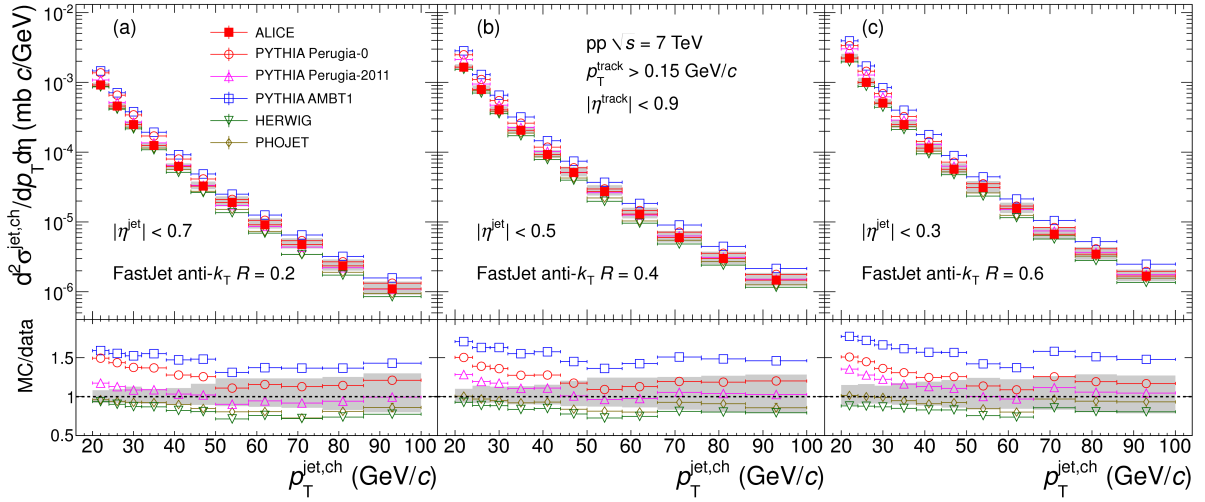


Fig. 5: (Color online) Top panels: Charged jet cross sections measured in the ALICE experiment in pp collisions at  $\sqrt{s} = 7$  TeV compared to several MC generators: PYTHIA AMBT1, PYTHIA Perugia-0 tune, PYTHIA Perugia-2011 tune, HERWIG, and PHOJET. Bottom panels: Ratios MC/Data. Shaded bands show quadratic sum of statistical and systematic uncertainties on the data drawn at unity.

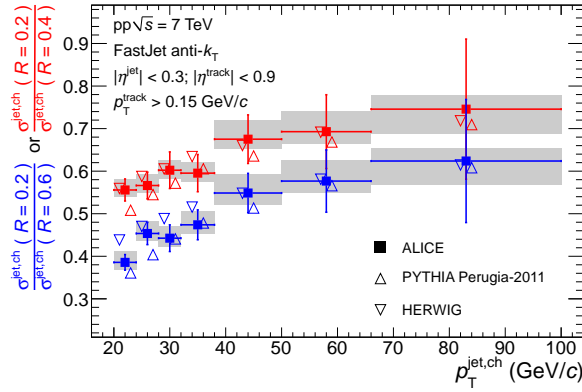


Fig. 6: (Color online) Ratios of jet cross sections for charged jets reconstructed using anti- $k_T$  algorithm with resolution parameters 0.2 and 0.4 and 0.2 and 0.6. The jet acceptance is restricted to  $|\eta^{\text{jet}}| \leq 0.3$ . The ratios in data are compared to PYTHIA Perugia-2011 and HERWIG simulations.

493 systematically underestimate the measured particle multiplicities particularly at the largest  $R$  for smaller  
 494 jet momentum, whereas HERWIG tends to overpredict the data at smaller  $R$ . An overall agreement  
 495 between the data and MC predictions is found to be best with the Perugia-2011 tune and PHOJET.

#### 496 8.4 Transverse momentum density distributions within the leading jet

497 The left panels of Figs. 8, 9, and 10 show leading jets average  $p_T$  density radial distributions  $\langle dp_T^{\text{sum}}/dr \rangle$   
 498 measured with resolution parameters  $R = 0.2$ ,  $0.4$ , and  $0.6$ , respectively. The distributions are plotted  
 499 separately for jets in the  $p_T$  intervals 20 - 30, 30 - 40, 40 - 60, and 60 to 80 GeV/c. The latter three  
 500 distributions are scaled by factors of 10, 100, and 1000 respectively for clarity. The transverse momentum  
 501 density is largest near the jet axis and decreases approximately exponentially with increasing  $r$ . Densities  
 502 are largest at the highest jet  $p_T$  where they are also found to have the steepest dependence on  $r$ . This  
 503 indicates that high  $p_T$  jets are on average more collimated than low  $p_T$  jets as already hinted in Fig. 6.

504 The measured distributions are compared to predictions with MC models. The right panels of Figs. 8, 9,



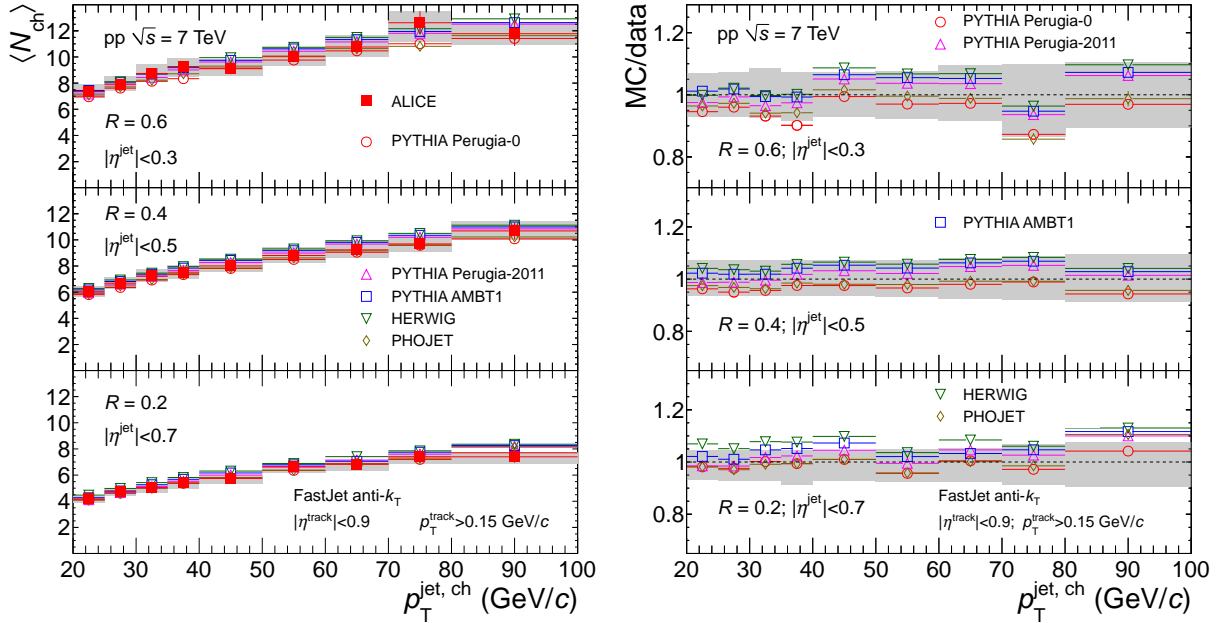


Fig. 7: (Color online) Left panel: Mean charged particle multiplicity in the leading charged jet as a function of jet  $p_T$  compared to MC models for pp collisions at  $\sqrt{s} = 7$  TeV for various jet resolution parameters ( $R = 0.6$  (left top),  $R = 0.4$  (left middle) and  $R = 0.2$  (left bottom)). UE contributions are subtracted from both data and MC. Right panel: Ratios MC/data. Shaded bands show the quadratic sum of statistical and systematic uncertainties on the data drawn at unity.

505 and 10 display ratios of the model calculations to measured data. The MC models qualitatively reproduce  
 506 the magnitude of the measured densities as well as their radial dependence. The agreement between the  
 507 MC model calculations and data is better at smaller  $R$  ( $= 0.2$ ). At  $R = 0.4$  and  $0.6$  HERWIG and Perugia-  
 508 0 tune of PYTHIA tend to underpredict the measured transverse momentum density except at small  $r$   
 509 for the two lowest jet  $p_T$  bins. The excess over the data for the smallest  $r$  and the slope of the ratio of  
 510 simulations to data observed for  $R = 0.6$  indicates stronger jet collimation for low  $p_T$  jets than observed in  
 511 the data. This observation is consistent with the discrepancy of the Herwig model to the measured cross  
 512 section ratio discussed in Sec. 8.2 (see also Fig. 6). In the last bin of Figs. 9, and 10 (right panel), large  
 513 deviations of MC models (PHOJET and HERWIG) from the data are found, whereas good agreement is  
 514 observed when data and simulations are not corrected for the UE contribution (not shown). This indicates  
 515 that the UE is underestimated by these models, as reported in [52] for PHOJET and in [50] for HERWIG  
 516 simulations of the UE density of charged and neutral particles with  $p_T > 0.5$  GeV/c.

### 517 8.5 Leading charged jet size

518 The left panel of Fig. 11 displays measured distributions of the average radius,  $\langle R_{80} \rangle$ , containing 80% of  
 519 the total jet  $p_T$  observed in jet cones with  $R = 0.2, 0.4$ , and  $0.6$ . The distributions are corrected using the  
 520 bin-by-bin method described in Sec. 6.1 to account for instrumental effects. No corrections are applied  
 521 for UE contributions, which are estimated to have a negligible effects on measured  $\langle R_{80} \rangle$  values. Jet  
 522 widths are largest at the lowest measured  $p_T$  and decrease monotonically with increasing  $p_T$ , indicating  
 523 that high  $p_T$  jets are more collimated than low  $p_T$  jets (as observed in Figs. 6, 8, 9, and 10) in a similar  
 524 way as predicted by various MC models and in qualitative agreement with prior measurement by the  
 525 CDF [8] collaboration.

526 Figure 11 also displays  $\langle R_{80} \rangle$  distributions predicted by PYTHIA (tunes Perugia-0, Perugia-2011, AMBT1),  
 527 PHOJET, and HERWIG. All five models qualitatively reproduce the observed magnitude and  $p_T$  dependence  
 528 of  $\langle R_{80} \rangle$  at  $R = 0.2$  and  $0.4$ . However, at  $R = 0.6$ , HERWIG, PHOJET, and PYTHIA Perugia-0

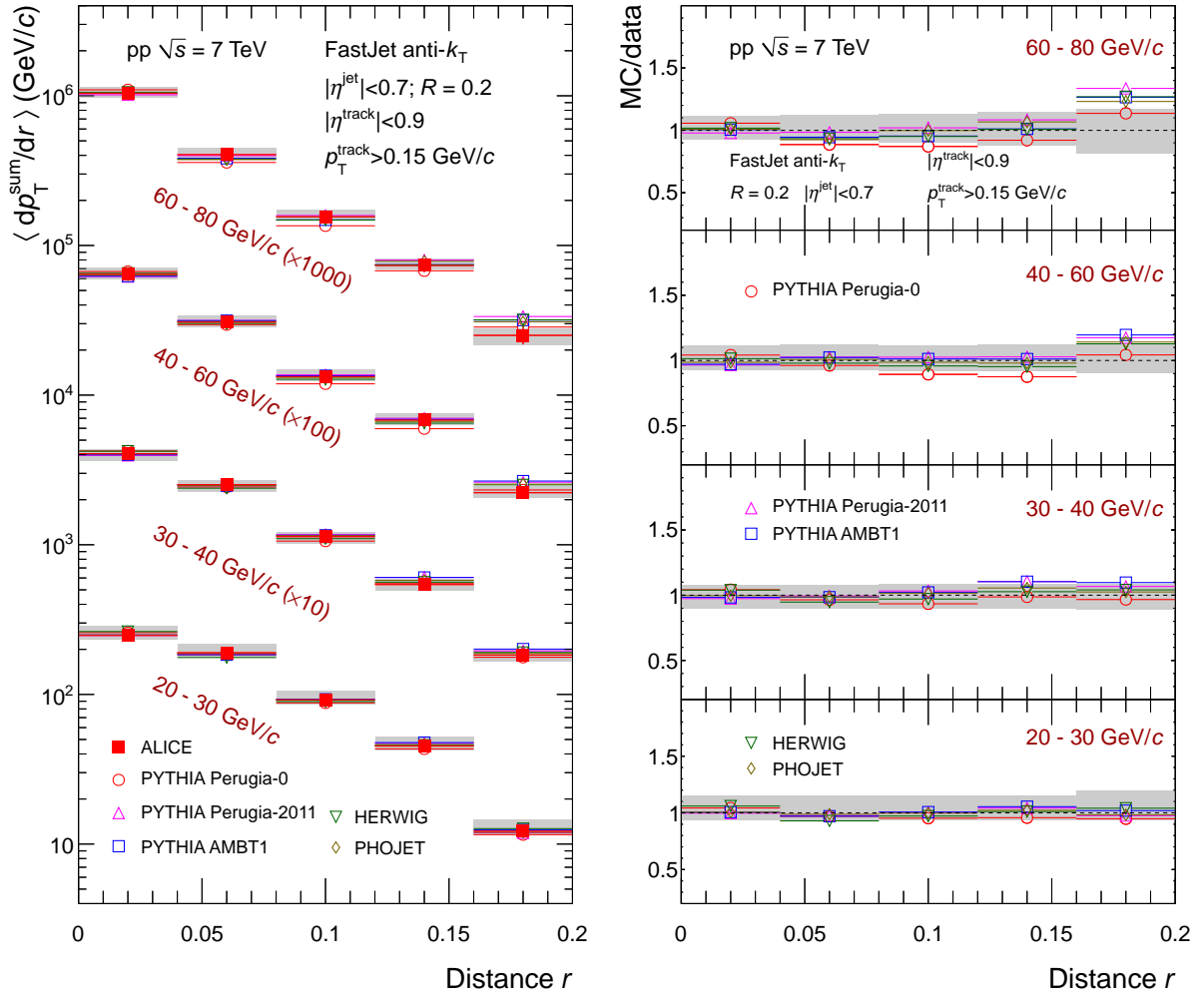


Fig. 8: (Color online) Left panel: Radial distributions of  $p_T$  density as a function radial distance 'r' from the jet direction for leading charged jets reconstructed with resolution parameter  $R = 0.2$  for selected jet  $p_T$  ranges in pp collisions at  $\sqrt{s} = 7$  TeV. Measured distributions are compared to MC model calculations. UE contributions are subtracted from both data and MC. Right panel: Ratios MC/data. Shaded bands show the quadratic sum of statistical and systematic uncertainties of the data drawn at unity.

529 tune systematically underpredict the data at low  $p_T$ . The PYTHIA tunes Perugia-2011 and AMBT1 are  
 530 in best agreement with the measured values.

## 531 8.6 Jet fragmentation

532 The left panels of Figs. 12, 13, and 14 present the measured  $p_T$  spectra  $F^{p_T}$  and scaled  $p_T$  spectra  $F^z$  and  
 533  $F^\xi$  of charged particles in leading charged jets reconstructed with a resolution parameter  $R = 0.4$ . The  
 534 data are corrected for instrumental effects, UE background, and contamination from secondary particles.  
 535 Systematic uncertainties, indicated by the shaded bands, include the detector response, UE subtraction,  
 536 correction for secondaries and event generator dependence.

537 The particle momentum distributions  $F^{p_T}$  are shown for four bins in jet transverse momentum: 20 - 30,  
 538 30 - 40, 40 - 60, and 60 - 80 GeV/c. The latter three are scaled by factors of 10, 100, and 1000 respectively  
 539 for clarity. The  $p_T$  spectra of the jet constituents span 2 - 3 orders of magnitude. The slopes are steepest  
 540 for the lowest  $p_T$  jets and progressively flatter with increasing jet  $p_T$ . This dependence is essentially  
 541 driven by the jet energy scale, as illustrated in Fig. 13, which displays fragmentation distributions  $F^z$  for

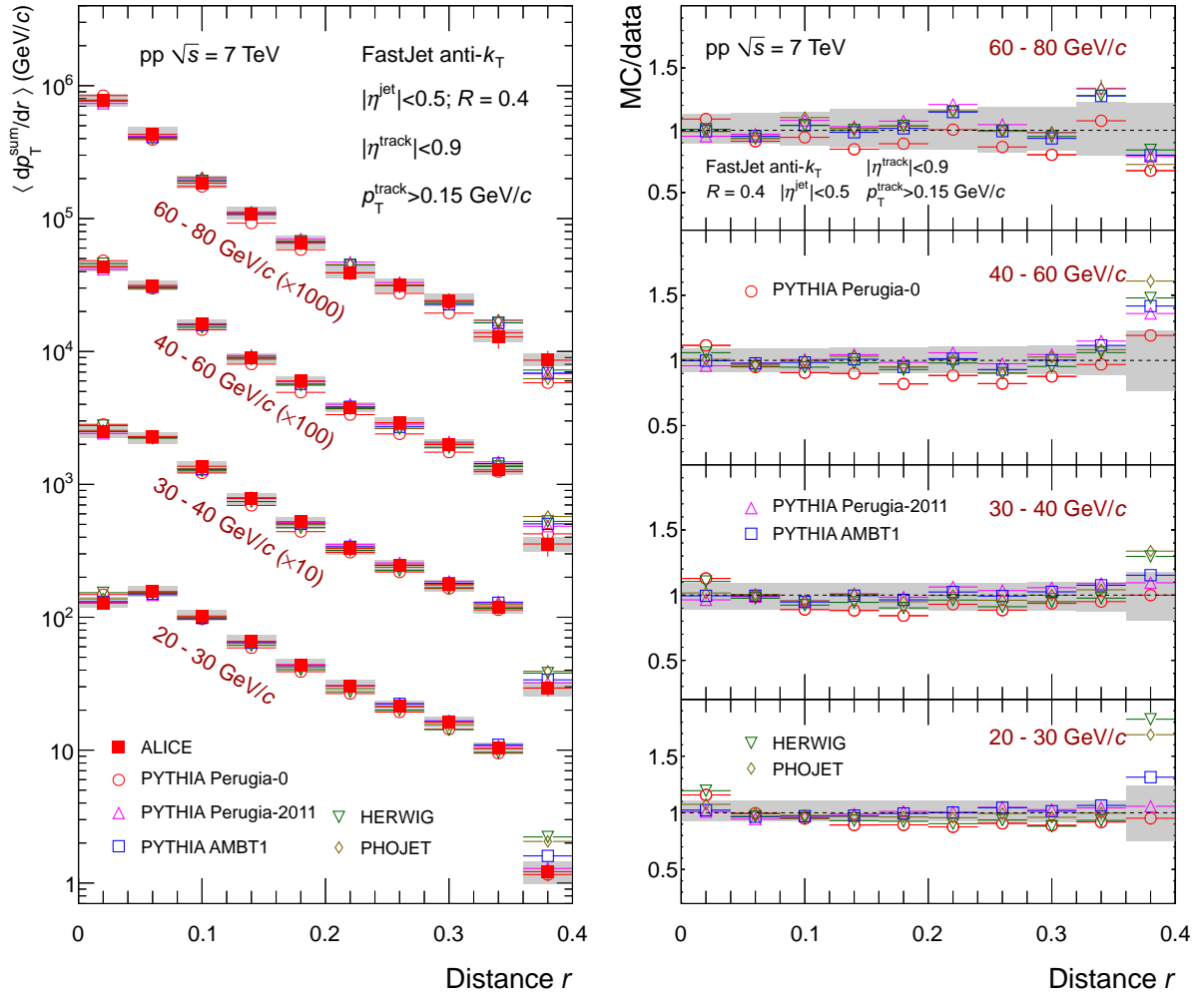


Fig. 9: (Color online) Same as Fig. 8 for a resolution parameter  $R = 0.4$ .

542 jets in the same four jet momentum ranges. For  $z^{\text{ch}} > 0.1$  all measured distributions are consistent within  
 543 uncertainties, indicating a scaling of charged jet fragmentation with charged jet transverse momentum.

544 The fragmentation distributions  $F^\xi$ , shown in Fig. 14, resolve in more detail the differences observed for  
 545 small values of  $z^{\text{ch}}$ . For small values of  $\xi^{\text{ch}} \lesssim 2$ , the distributions exhibit the approximate scaling already  
 546 seen for  $F^z$ , whereas at higher  $\xi^{\text{ch}}$ , corresponding to small  $z^{\text{ch}}$ , a pronounced maximum ('hump-backed  
 547 plateau') is observed, indicating the suppression of low momentum particle production by QCD coher-  
 548 ence [35]. With increasing jet transverse momentum, the area of the distributions increases, showing the  
 549 rise of particle multiplicity in jets (as observed in Fig. 7), and the maximum shifts to higher values of  
 550  $\xi^{\text{ch}}$ . This observation is in qualitative agreement with full di-jet fragmentation functions measured in  
 551  $p\bar{p}$  collisions at  $\sqrt{s} = 1.8 \text{ TeV}$  [14] and with expectations from QCD calculations based on the Modified  
 552 Leading Logarithmic Approximation (MLLA) [58].

553 The measured fragmentation distributions are compared to calculations obtained from the HERWIG [19],  
 554 PHOJET [20] and PYTHIA [18] event generators and the ratios of the calculated MC distributions to  
 555 measured distributions are shown in the right panels of Figs. 12, 13, and 14. The UE contributions to MC  
 556 events are estimated and subtracted using perpendicular cones pointing into the event transverse region  
 557 as described in Sec. 6.4. At high particle transverse momenta and high  $z^{\text{ch}}$ , the data and simulations  
 558 agree within uncertainties, except for the two lowest jet  $p_T$  bins, where the measured yield seems to be  
 559 systematically higher than the simulations with PYTHIA tunes Perugia-2011 and AMBT1 for  $z^{\text{ch}} > 0.6$ .

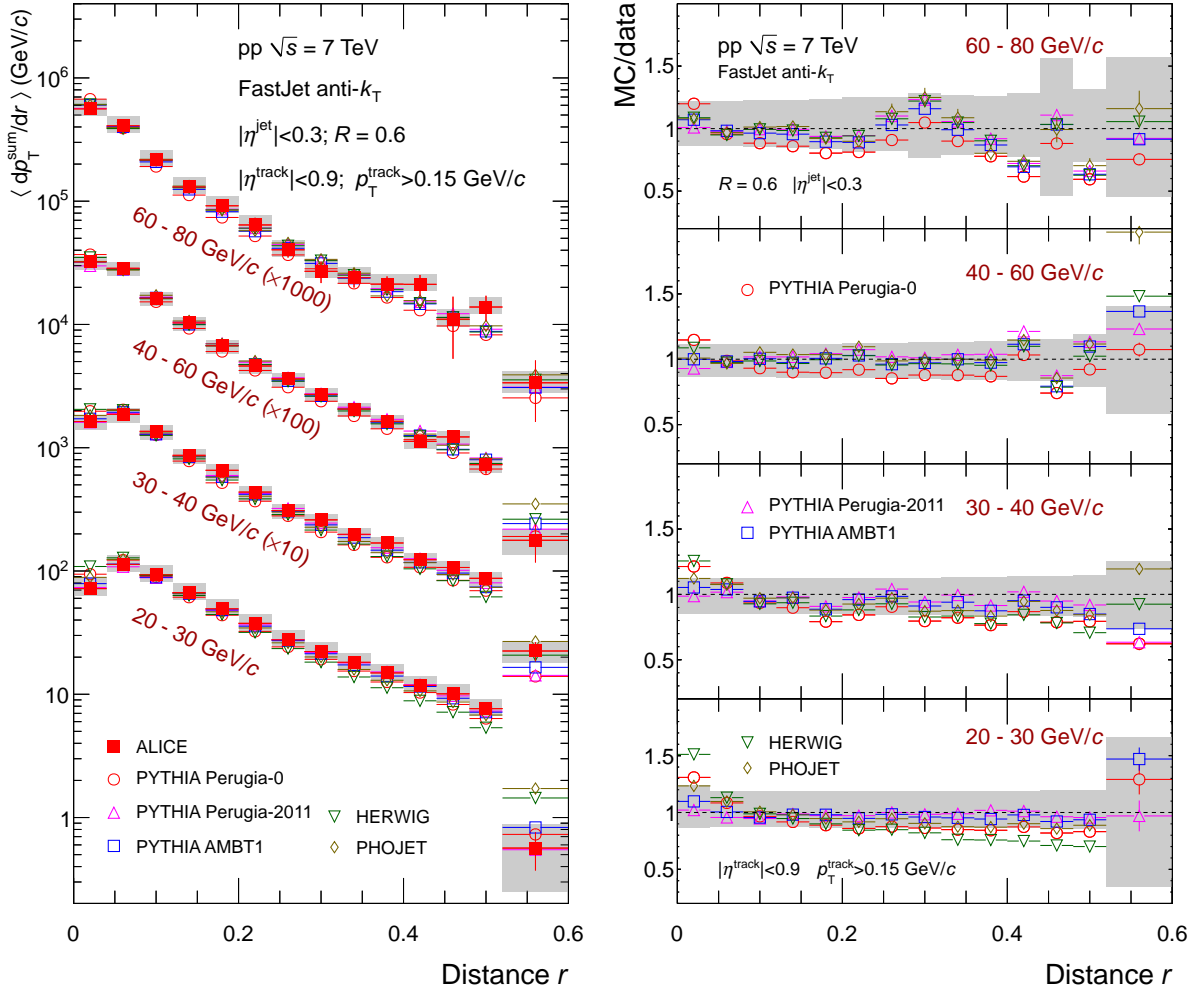


Fig. 10: (Color online) Same as Fig. 8 for a resolution parameter  $R = 0.6$ .

560 In the low momentum / high  $\xi^{\text{ch}}$  region, the measured yield is systematically larger than produced by  
 561 the PYTHIA and PHOJET simulations. To investigate the discrepancy at low particle momentum, data  
 562 and simulations are also compared without subtraction of the UE (not shown). In this case, the excess  
 563 of low momentum constituents in data over PYTHIA simulations is still significant, however reduced in  
 564 magnitude and comparable to other measurements at higher constituent momenta [3]. It is thus concluded  
 565 that in the PYTHIA tunes investigated in this work the UE contribution to the low momentum particle  
 566 yield is overestimated relative to the contribution from hard parton fragmentation. The data at low  $p_{\text{T}}$   
 567 are best described by the HERWIG event generator, which hints to a sensitivity of the low momentum  
 568 fragmentation to the details of the parton shower model in the simulations.

## 569 9 Summary and conclusion

570 In summary, we reported measurements of the inclusive charged particle jet cross section, jet fragmen-  
 571 tation and jet shapes at midrapidity in pp collisions at  $\sqrt{s} = 7$  TeV using the ALICE detector at the  
 572 LHC.

573 Jets were reconstructed with infrared and collinear safe jet finding algorithms,  $k_{\text{T}}$ , anti- $k_{\text{T}}$  and a seedless  
 574 infrared safe iterative cone based algorithm, SIS Cone. As the measured inclusive jet spectra did not  
 575 show any significant dependence on the jet algorithm used, all observables discussed throughout the  
 576 paper were based on jets reconstructed with the anti- $k_{\text{T}}$  sequential recombination algorithm, commonly

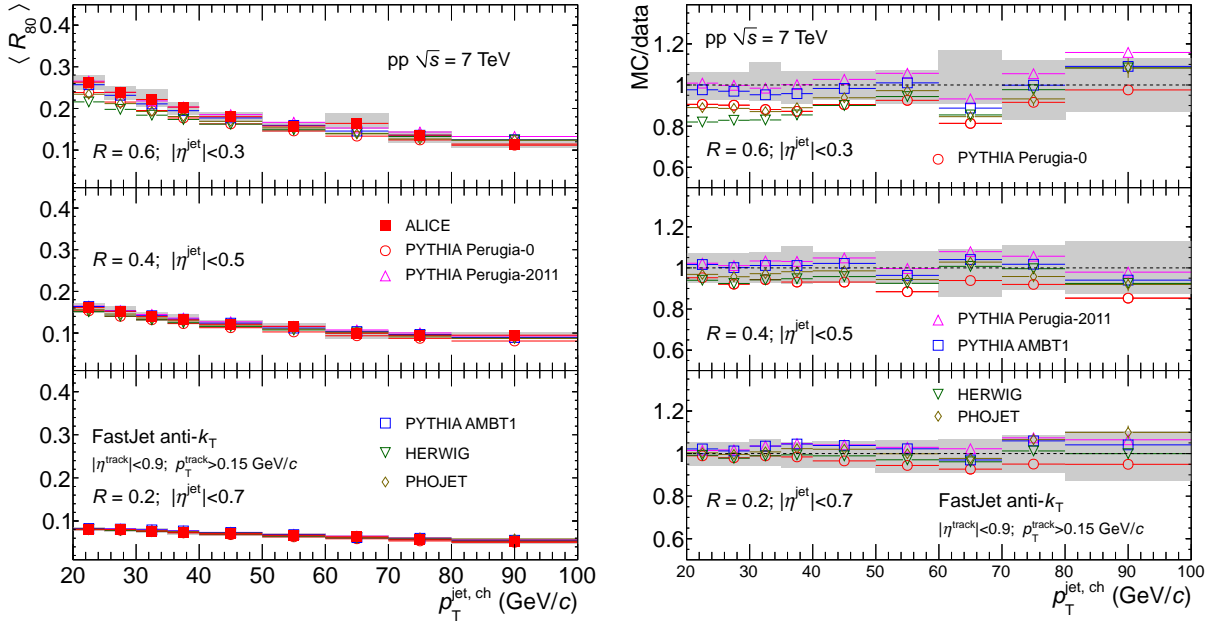


Fig. 11: (Color online) Left panel: Distributions of average radius  $\langle R_{80} \rangle$  containing 80% of the  $p_T$  with respect to the total reconstructed jet  $p_T$  as a function of jet  $p_T$  compared to MC models for pp collisions at  $\sqrt{s} = 7$  TeV for various jet resolution parameters ( $R = 0.6$  (left top),  $R = 0.4$  (left middle) and  $R = 0.2$  (left bottom)). Right panel: Ratios MC/data. Shaded bands show quadratic sum of the statistical and systematic uncertainties of the data drawn at unity.

577 utilized in the LHC community. In order to gain as much information as possible, the anti- $k_T$  algorithm  
 578 was run with several resolution parameters  $R$  ranging from 0.2 to 0.6.

579 The inclusive charged jet cross section was measured in the  $p_T^{\text{jet, ch}}$  interval from 20 to 100 GeV/c and  
 580 found to be consistent with the ATLAS measurement at the same collision energy. The ratios of jet  
 581 cross sections for resolution parameter  $R = 0.2$  over  $R = 0.4$  and 0.6, respectively, are found to increase  
 582 with increasing  $p_T$  of jets, pointing toward an increasing collimation of particles in jets around the jet  
 583 axis. This finding, expected by pQCD calculations, is corroborated by a detailed study of  $\langle R_{80} \rangle$  variable  
 584 defined as the average radius containing 80% of total charged jet  $p_T$ . The  $p_T$  density is found to be  
 585 the largest near the jet axis and decreases radially away from the jet axis. This radial decrease is found  
 586 to be larger for high  $p_T$  jets which are more collimated. The averaged charged particle multiplicity  
 587 in jets ( $\langle N_{ch} \rangle$ ) increases with jet momentum and resolution parameter  $R$ . We studied charged particle  
 588 fragmentation in leading charged jets. The scaled  $p_T$  spectra of charged particles associated with jets  
 589 exhibit a pronounced maximum commonly referred to as ‘hump-backed plateau’ consistent with the  
 590 suppression of low momentum particle production by QCD coherence. The area of the distribution  
 591 increases with jet  $p_T$  and reflects the observed increase of  $\langle N_{ch} \rangle$  discussed above. The observed behaviour  
 592 is in qualitative agreement with MLLA [58] calculations and earlier measurements [14] in  $p\bar{p}$  collisions at  
 593 the Tevatron ( $\sqrt{s} = 1.8$  TeV). The jet fragmentation distributions for the measured jet  $p_T$  ranges indicate  
 594 a scaling of charged jet fragmentation with jet  $p_T$  for  $z^{\text{ch}} > 0.1$ .

595 All measured observables were also compared to several MC generators (PYTHIA, PHOJET, HERWIG).  
 596 None of the generators gives a perfect description of the measured charged jet cross section. PHOJET  
 597 and most of the PYTHIA tunes used in this work overestimate the cross section. PYTHIA Perugia-2011  
 598 agrees reasonably well with the data for intermediate and high charged jet  $p_T$ , whereas HERWIG re-  
 599 produces best the cross section at low jet  $p_T$ . The jet properties are reproduced rather well by the MC  
 600 generators. The agreement of the calculations with the data for observables  $\langle N_{ch} \rangle$ ,  $\langle R_{80} \rangle$ , and radial  $p_T$   
 601 density is typically at the level of 5-10%. In case of the fragmentation functions, the data are better

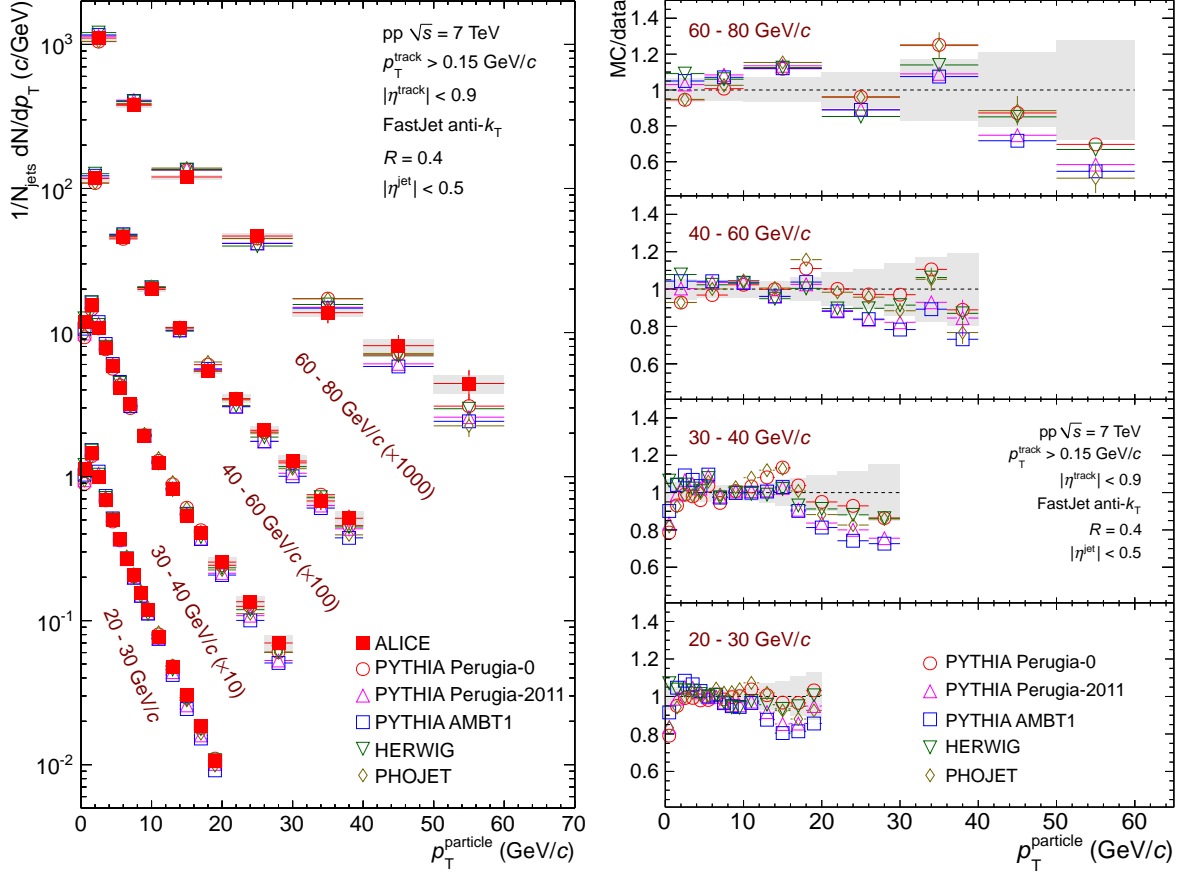


Fig. 12: (Color online) Left panel: Charged particle  $p_T$  spectra  $dN/dp_T$  in leading jets for different bins in jet transverse momentum, compared to simulations. For simulations and data, the UE contribution is subtracted. Right panel: Ratio of simulations to data. The shaded band indicates the quadratic sum of statistical and systematic uncertainties on the data.

602 described by the HERWIG event generator. The high momentum (low  $\xi^{\text{ch}}$ ) region is relatively well de-  
 603 scribed by the generators, while for the low momenta (high  $\xi^{\text{ch}}$ ), the measured yield significantly exceeds  
 604 PHOJET and PYTHIA predictions. We emphasize the relevance of this observation for the choice of a  
 605 generator based pp reference for future measurements of jet fragmentation in nuclear collisions, where  
 606 similar effects are predicted as a signature of parton energy loss in the hot and dense strongly-interacting  
 607 medium.

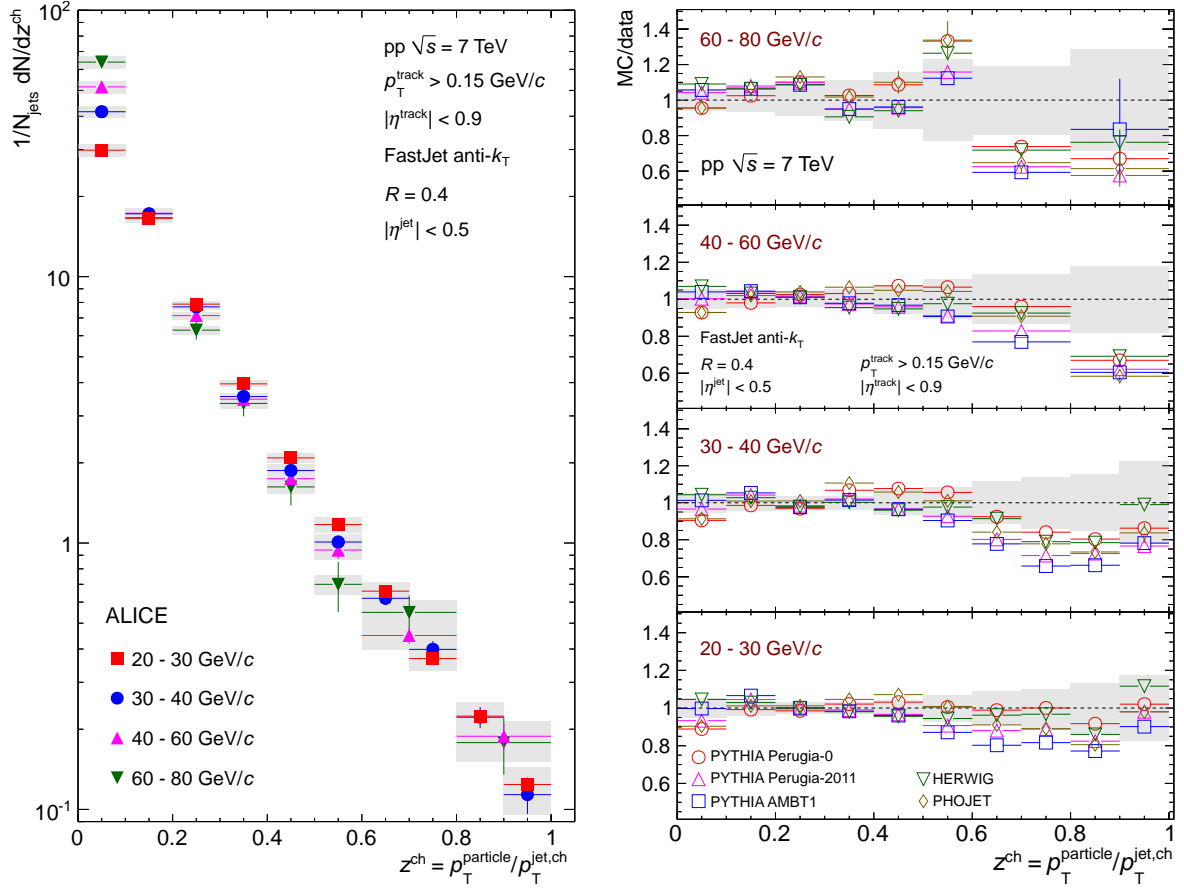


Fig. 13: (Color online) Left panel: Charged particle scaled  $p_{\text{T}}$  spectra  $dN/dz^{\text{ch}}$  in leading jets for different bins in jet transverse momentum, compared to simulations. For simulations and data, the UE contribution is subtracted. Right panel: Ratio of simulations to data. The shaded band indicates the quadratic sum of statistical and systematic uncertainties on the data.

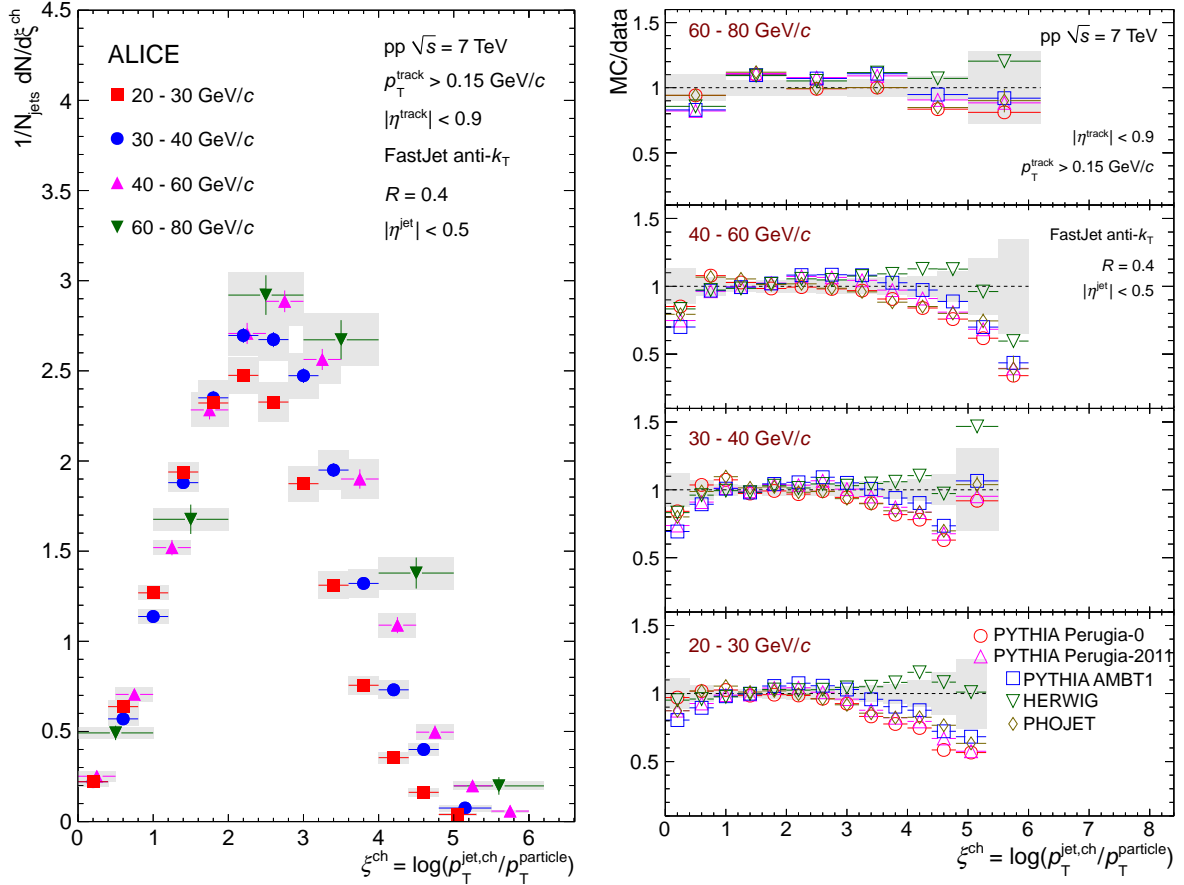


Fig. 14: (Color online) Left panel: Charged particle scaled  $p_{\text{T}}$  spectra  $dN/d\xi^{\text{ch}}$  in leading jets for different bins in jet transverse momentum, compared to simulations. For simulations and data, the UE contribution is subtracted. Right panel: Ratio of simulations to data. The shaded band indicates the quadratic sum of statistical and systematic uncertainties on the data.



## References

- [1] B. Abbott *et al.* (D0 Collaboration), Phys. Rev. Lett. **82**, 2451 (1999); Phys. Rev. Lett. **86**, 2523 (2001); V. M. Abazov *et al.* (D0 Collaboration), Phys. Rev. Lett. **101**, 062001 (2008).
- [2] F. Abe *et al.* (CDF Collaboration), Phys. Rev. Lett. **68**, 1104 (1992); Phys. Rev. Lett. **70**, 1376 (1993); Phys. Rev. Lett. **77**, 438 (1996); T. Affolder *et al.* (CDF Collaboration), Phys. Rev. D **64**, 032001 (2001); A. Abulencia *et al.* (CDF Collaboration), Phys. Rev. Lett. **96**, 122001 (2006).
- [3] G. Aad *et al.* (ATLAS Collaboration), Phys. Rev. D **84**, 054001 (2011).
- [4] G. Aad *et al.* (ATLAS Collaboration), Phys. Rev. D **86**, 014022 (2012).
- [5] S. Chatrchyan *et al.* (CMS Collaboration), Phys. Rev. Lett. **107**, 132001 (2011); Phys. Rev. D **87**, 112002 (2013).
- [6] B. Abelev *et al.* (ALICE Collaboration), Phys. Lett. B **722**, 262-267, (2013).
- [7] F. Abe *et al.* (CDF Collaboration), Phys. Rev. Lett. **70**, 713 (1993).
- [8] T. Affolder *et al.* (CDF Collaboration), Phys. Rev. D **65**, 092002 (2001).
- [9] D. Acosta *et al.* (CDF Collaboration), Phys. Rev. D **71**, 112002 (2005).
- [10] S. Abachi *et al.* (D0 Collaboration), Phys. Lett. B **357**, 500 (1995).
- [11] G. Aad *et al.* (ATLAS Collaboration), Phys. Rev. D **83**, 052003 (2011).
- [12] S. Chatrchyan *et al.* (CMS Collaboration), JHEP **06**, 160 (2012).
- [13] S. Chatrchyan *et al.* (CMS Collaboration), Phys. Lett. B **730**, 243 (2014).
- [14] D. Acosta *et al.* (CDF Collaboration), Phys. Rev. D **68**, 012003 (2003).
- [15] G. Aad *et al.* (ATLAS Collaboration), Eur. Phys. J. C **71**, 1795 (2011).
- [16] The ATLAS Collaboration, ATLAS-CONF-2012-115 (2012).
- [17] S. Chatrchyan *et al.* (CMS Collaboration), JHEP **10**, 087 (2012).
- [18] T. Sjostrand, S. Mrenna, P.Z. Skands, JHEP **05**, 026 (2006).
- [19] G. Marchesini, B. R. Webber, G. Abbiendi, I. G. Knowles, M. H. Seymour and L. Stanco, Computer Physics Communications **67**, 465 (1992); G. Corcella, I. G. Knowles, G. Marchesini, S. Moretti, K. Odagiri, P. Richardson, M.H. Seymour and B.R. Webber, JHEP **0101**, 010 (2001).
- [20] S. Roesler, R. Engel, J. Ranft, Lisbon 2000 - Advanced Monte Carlo (2000), 1033-1038 [*hep-ph/0012252*]
- [21] K. Aamodt *et al.* (ALICE Collaboration), JHEP **1403**, 013 (2014).
- [22] J. Beringer *et al.* (Particle Data Group), Phys. Rev. D **86**, 010001 (2012) and 2013 partial update for the 2014 edition.
- [23] K. C. Zapp, F. Krauss, U. A. Wiedemann, JHEP **1303**, 080 (2013).
- [24] S. Sapeta, U. A. Wiedemann, Eur. Phys. J. C **55**, 293 (2007).
- [25] T. Renk, Nucl. Phys. A **904**, 725 (2013).
- [26] K. Aamodt *et al.* (ALICE Collaboration), JINST **3**, 508002 (2008).
- [27] J. Alme, Y. Andres, H. Appelshäuser, S. Boblok, N. Bialas *et al.*, Nucl. Instrum. Meth. A **622**, 316 (2010).
- [28] K. Aamodt *et al.* (ALICE Collaboration), JINST **5**, P03003 (2010).
- [29] ALICE Collaboration, CERN-LHCC-2004-025; <http://cdsweb.cern.ch/record/781854>
- [30] K. Aamodt *et al.* (ALICE Collaboration), Eur. Phys. J. C **73**, 2456 (2013).
- [31] M. Cacciari, G. P. Salam, G. Soyez, JHEP **04**, 63 (2008).
- [32] S. Catani, Y. L. Dokshitzer, M. H. Seymour, B. R. Webber, Nucl. Phys. B **406**, 187 (1993); S. D. Ellis, D. E. Soper, Phys. Rev. D **48**, 3160 (1993).
- [33] M. Cacciari, G. P. Salam, Phys. Lett. B **641**, 57 (2006).
- [34] G. P. Salam, G. Soyez, JHEP **0705**, 086 (2007).

- 653 [35] B. I. Ermolayev, V. S. Fadin, JETP Lett. **33**, 285 (1981); A. H. Mueller, Phys. Lett. B **104**, 161  
654 (1981).
- 655 [36] P. Z. Skands, Phys. Rev. D **82**, 074018 (2010)  
656 [*hep-ph/1005.3457*].
- 657 [37] R. Brun, F. Carminati and S. Giani, CERN-W5013, 1994.
- 658 [38] T. Sjöstrand, P.Z. Skands, Eur. Phys. J. C **39**, 129 (2005).
- 659 [39] B. Andersson, G. Gustafson, B. Söderberg, Z. Phys. C **20** 137 (1983).
- 660 [40] ATLAS Collaboration, ATLAS-CONF-2010-031 (2010).
- 661 [41] H.L. Lai *et al.* (The CTEQ Collaboration), Eur. Phys. J. C **12**, 375 (2000).
- 662 [42] A. Sherstnev and R. S. Thorne, Eur. Phys. J C **55** 553 (2008).
- 663 [43] M. Gluck, E. Reya, A. Vogt, Z. Phys. C **67**, 433 (1995).
- 664 [44] G. D'Agostini, Nucl. Inst. Meth. A **362**, 487 (1995).
- 665 [45] A. Höcker, V. Kartvelishvili, Nucl. Inst. Meth. A **372**, 469 (1996).
- 666 [46] [http://hepunix.rl.ac.uk/adye/software/unfold/](http://hepunix.rl.ac.uk/adye/software/unfold/RooUnfold.html)  
667 *RooUnfold.html*
- 668 [47] V. Khachatryan *et al.* (CMS collaboration), JHEP **05** (2011) 064.
- 669 [48] P. Skands *et al.*, <https://mcplots.cern.ch>
- 670 [49] G. Aad *et al.* (ATLAS Collaboration), Phys. Rev. D **83**, 112001 (2011).
- 671 [50] G. Aad *et al.* (ATLAS Collaboration), Eur. Phys. J C **71** 1636 (2011).
- 672 [51] S. Chatrchyan *et al.* (CMS Collaboration), JHEP **09**, 109 (2011).
- 673 [52] B. Abelev *et al.* (ALICE Collaboration), JHEP **1207**, 116 (2012).
- 674 [53] B. Abelev *et al.* (ALICE Collaboration), Phys. Lett. B **720**, 52 (2013).
- 675 [54] B. Abelev *et al.* (ALICE Collaboration), Eur. Phys. J. C **73**, 2456 (2013); K. Oyama for the ALICE  
676 Collaboration, arXiv:1305.7044 [nucl-ex].
- 677 [55] A. Cruz *et al.*, CDF/ANAL/CDF/CDFR/7703 (2005).
- 678 [56] C. Tsallis, J. Stat. Phys. **52**, 479 (1988); Eur. Phys. J. A **40** (2009) 257; cf. also C. Tsallis, *Introduc-*  
679 *tion to Nonextensive Statistical Mechanics* (Berlin 2009: Springer). For an updated bibliography on  
680 this subject, see <http://tsallis.cat.cbpf.br/biblio.htm>.
- 681 [57] B. Abelev *et al.* (ALICE Collaboration), JHEP **03** 013 (2014).
- 682 [58] Y. L. Dokshitzer, S. Troyan, Proc. XIX winter School of the LNPI, 1984, Vol. I, p. 144.

## 683 Acknowledgements

684 The ALICE Collaboration would like to thank all its engineers and technicians for their invaluable con-  
685 tributions to the construction of the experiment and the CERN accelerator teams for the outstanding  
686 performance of the LHC complex.

687 The ALICE Collaboration gratefully acknowledges the resources and support provided by all Grid cen-  
688 tres and the Worldwide LHC Computing Grid (WLCG) collaboration.

689 The ALICE Collaboration acknowledges the following funding agencies for their support in building and  
690 running the ALICE detector:

691 State Committee of Science, World Federation of Scientists (WFS) and Swiss Fonds Kidagan, Armenia,  
692 Conselho Nacional de Desenvolvimento Científico e Tecnológico (CNPq), Financiadora de Estudos e  
693 Projetos (FINEP), Fundação de Amparo à Pesquisa do Estado de São Paulo (FAPESP);

694 National Natural Science Foundation of China (NSFC), the Chinese Ministry of Education (CMOE) and  
695 the Ministry of Science and Technology of China (MSTC);

696 Ministry of Education and Youth of the Czech Republic;

697 Danish Natural Science Research Council, the Carlsberg Foundation and the Danish National Research

698 Foundation;  
699 The European Research Council under the European Community's Seventh Framework Programme;  
700 Helsinki Institute of Physics and the Academy of Finland;  
701 French CNRS-IN2P3, the 'Region Pays de Loire', 'Region Alsace', 'Region Auvergne' and CEA,  
702 France;  
703 German BMBF and the Helmholtz Association;  
704 General Secretariat for Research and Technology, Ministry of Development, Greece;  
705 Hungarian OTKA and National Office for Research and Technology (NKTH);  
706 Department of Atomic Energy and Department of Science and Technology of the Government of India;  
707 Istituto Nazionale di Fisica Nucleare (INFN) and Centro Fermi - Museo Storico della Fisica e Centro  
708 Studi e Ricerche "Enrico Fermi", Italy;  
709 MEXT Grant-in-Aid for Specially Promoted Research, Japan;  
710 Joint Institute for Nuclear Research, Dubna;  
711 National Research Foundation of Korea (NRF);  
712 CONACYT, DGAPA, México, ALFA-EC and the EPLANET Program (European Particle Physics Latin  
713 American Network)  
714 Stichting voor Fundamenteel Onderzoek der Materie (FOM) and the Nederlandse Organisatie voor  
715 Wetenschappelijk Onderzoek (NWO), Netherlands;  
716 Research Council of Norway (NFR);  
717 Polish Ministry of Science and Higher Education;  
718 National Science Centre, Poland;  
719 Ministry of National Education/Institute for Atomic Physics and CNCS-UEFISCDI - Romania;  
720 Ministry of Education and Science of Russian Federation, Russian Academy of Sciences, Russian Fed-  
721 eral Agency of Atomic Energy, Russian Federal Agency for Science and Innovations and The Russian  
722 Foundation for Basic Research;  
723 Ministry of Education of Slovakia;  
724 Department of Science and Technology, South Africa;  
725 CIEMAT, EELA, Ministerio de Economía y Competitividad (MINECO) of Spain, Xunta de Galicia  
726 (Consellería de Educación), CEADEN, Cubaenergía, Cuba, and IAEA (International Atomic Energy  
727 Agency);  
728 Swedish Research Council (VR) and Knut & Alice Wallenberg Foundation (KAW);  
729 Ukraine Ministry of Education and Science;  
730 United Kingdom Science and Technology Facilities Council (STFC);  
731 The United States Department of Energy, the United States National Science Foundation, the State of  
732 Texas, and the State of Ohio;  
733 Ministry of Science, Education and Sports of Croatia and Unity through Knowledge Fund, Croatia.

734 **A The ALICE Collaboration**

735 B. Abelev<sup>71</sup>, J. Adam<sup>37</sup>, D. Adamová<sup>79</sup>, M.M. Aggarwal<sup>83</sup>, G. Aglieri Rinella<sup>34</sup>, M. Agnello<sup>107,90</sup>,  
736 A. Agostinelli<sup>26</sup>, N. Agrawal<sup>44</sup>, Z. Ahammed<sup>126</sup>, N. Ahmad<sup>18</sup>, I. Ahmed<sup>15</sup>, S.U. Ahn<sup>64</sup>, S.A. Ahn<sup>64</sup>,  
737 I. Aimo<sup>90,107</sup>, S. Aiola<sup>131</sup>, M. Ajaz<sup>15</sup>, A. Akindinov<sup>54</sup>, S.N. Alam<sup>126</sup>, D. Aleksandrov<sup>96</sup>, B. Alessandro<sup>107</sup>,  
738 D. Alexandre<sup>98</sup>, A. Alici<sup>101,12</sup>, A. Alkin<sup>3</sup>, J. Alme<sup>35</sup>, T. Alt<sup>39</sup>, S. Altinpinar<sup>17</sup>, I. Altsybeev<sup>125</sup>,  
739 C. Alves Garcia Prado<sup>115</sup>, C. Andrei<sup>74</sup>, A. Andronic<sup>93</sup>, V. Anguelov<sup>89</sup>, J. Anielski<sup>50</sup>, T. Antičić<sup>94</sup>,  
740 F. Antinori<sup>104</sup>, P. Antonioli<sup>101</sup>, L. Aphecetche<sup>109</sup>, H. Appelshäuser<sup>49</sup>, S. Arcelli<sup>26</sup>, N. Armesto<sup>16</sup>,  
741 R. Arnaldi<sup>107</sup>, T. Aronsson<sup>131</sup>, I.C. Arsene<sup>93,21</sup>, M. Arslandok<sup>49</sup>, A. Augustinus<sup>34</sup>, R. Averbeck<sup>93</sup>,  
742 T.C. Awes<sup>80</sup>, M.D. Azmi<sup>85,18</sup>, M. Bach<sup>39</sup>, A. Badalà<sup>103</sup>, Y.W. Baek<sup>66,40</sup>, S. Bagnasco<sup>107</sup>, R. Bailhache<sup>49</sup>,  
743 R. Bala<sup>86</sup>, A. Baldisseri<sup>14</sup>, F. Baltasar Dos Santos Pedrosa<sup>34</sup>, R.C. Baral<sup>57</sup>, R. Barbera<sup>27</sup>, F. Barile<sup>31</sup>,  
744 G.G. Barnaföldi<sup>130</sup>, L.S. Barnby<sup>98</sup>, V. Barret<sup>66</sup>, J. Bartke<sup>112</sup>, M. Basile<sup>26</sup>, N. Bastid<sup>66</sup>, S. Basu<sup>126</sup>,  
745 B. Bathen<sup>50</sup>, G. Batigne<sup>109</sup>, A. Batista Camejo<sup>66</sup>, B. Batyunya<sup>62</sup>, P.C. Batzing<sup>21</sup>, C. Baumann<sup>49</sup>,  
746 I.G. Bearden<sup>76</sup>, H. Beck<sup>49</sup>, C. Bedda<sup>90</sup>, N.K. Behera<sup>44</sup>, I. Belikov<sup>51</sup>, F. Bellini<sup>26</sup>, R. Bellwied<sup>117</sup>,  
747 E. Belmont-Moreno<sup>60</sup>, R. Belmont III<sup>129</sup>, V. Belyaev<sup>72</sup>, G. Bencedi<sup>130</sup>, S. Beole<sup>25</sup>, I. Berceanu<sup>74</sup>,  
748 A. Bercuci<sup>74</sup>, Y. Berdnikov<sup>ii,81</sup>, D. Berenyi<sup>130</sup>, M.E. Berger<sup>88</sup>, R.A. Bertens<sup>53</sup>, D. Berzano<sup>25</sup>, L. Betev<sup>34</sup>,  
749 A. Bhasin<sup>86</sup>, I.R. Bhat<sup>86</sup>, A.K. Bhati<sup>83</sup>, B. Bhattacharjee<sup>41</sup>, J. Bhom<sup>122</sup>, L. Bianchi<sup>25</sup>, N. Bianchi<sup>68</sup>,  
750 C. Bianchin<sup>53</sup>, J. Bielčik<sup>37</sup>, J. Bielčiková<sup>79</sup>, A. Bilandzic<sup>76</sup>, S. Bjelogrić<sup>53</sup>, F. Blanco<sup>10</sup>, D. Blau<sup>96</sup>,  
751 C. Blume<sup>49</sup>, F. Bock<sup>89,70</sup>, A. Bogdanov<sup>72</sup>, H. Bøggild<sup>76</sup>, M. Bogolyubsky<sup>108</sup>, F.V. Böhmer<sup>88</sup>, L. Boldizsár<sup>130</sup>,  
752 M. Bombara<sup>38</sup>, J. Book<sup>49</sup>, H. Borel<sup>14</sup>, A. Borissov<sup>92,129</sup>, M. Borri<sup>78</sup>, F. Bossú<sup>61</sup>, M. Botje<sup>77</sup>, E. Botta<sup>25</sup>,  
753 S. Böttger<sup>48</sup>, P. Braun-Munzinger<sup>93</sup>, M. Bregant<sup>115</sup>, T. Breitner<sup>48</sup>, T.A. Broker<sup>49</sup>, T.A. Browning<sup>91</sup>, M. Broz<sup>37</sup>,  
754 E. Bruna<sup>107</sup>, G.E. Bruno<sup>31</sup>, D. Budnikov<sup>95</sup>, H. Buesching<sup>49</sup>, S. Bufalino<sup>107</sup>, P. Buncic<sup>34</sup>, O. Busch<sup>89</sup>,  
755 Z. Buthelezi<sup>61</sup>, D. Caffarri<sup>34,28</sup>, X. Cai<sup>7</sup>, H. Caines<sup>131</sup>, L. Calero Diaz<sup>68</sup>, A. Caliva<sup>53</sup>, E. Calvo Villar<sup>99</sup>,  
756 P. Camerini<sup>24</sup>, F. Carena<sup>34</sup>, W. Carena<sup>34</sup>, J. Castillo Castellanos<sup>14</sup>, A.J. Castro<sup>120</sup>, E.A.R. Casula<sup>23</sup>,  
757 V. Catanescu<sup>74</sup>, C. Cavicchioli<sup>34</sup>, C. Ceballos Sanchez<sup>9</sup>, J. Cepila<sup>37</sup>, P. Cerello<sup>107</sup>, B. Chang<sup>118</sup>,  
758 S. Chapeland<sup>34</sup>, J.L. Charvet<sup>14</sup>, S. Chattopadhyay<sup>126</sup>, S. Chattopadhyay<sup>97</sup>, V. Chelnokov<sup>3</sup>, M. Cherney<sup>82</sup>,  
759 C. Cheshkov<sup>124</sup>, B. Cheynis<sup>124</sup>, V. Chibante Barroso<sup>34</sup>, D.D. Chinellato<sup>116,117</sup>, P. Chochula<sup>34</sup>, M. Chojnacki<sup>76</sup>,  
760 S. Choudhury<sup>126</sup>, P. Christakoglou<sup>77</sup>, C.H. Christensen<sup>76</sup>, P. Christiansen<sup>32</sup>, T. Chujo<sup>122</sup>, S.U. Chung<sup>92</sup>,  
761 C. Cicalo<sup>102</sup>, L. Cifarelli<sup>12,26</sup>, F. Cindolo<sup>101</sup>, J. Cleymans<sup>85</sup>, F. Colamaria<sup>31</sup>, D. Colella<sup>31</sup>, A. Collu<sup>23</sup>,  
762 M. Colocci<sup>26</sup>, G. Conesa Balbastre<sup>67</sup>, Z. Conesa del Valle<sup>47</sup>, M.E. Connors<sup>131</sup>, J.G. Contreras<sup>37,11</sup>,  
763 T.M. Cormier<sup>129,80</sup>, Y. Corrales Morales<sup>25</sup>, P. Cortese<sup>30</sup>, I. Cortés Maldonado<sup>2</sup>, M.R. Cosentino<sup>115</sup>, F. Costa<sup>34</sup>,  
764 P. Crochet<sup>66</sup>, R. Cruz Albino<sup>11</sup>, E. Cuautle<sup>59</sup>, L. Cunqueiro<sup>34,68</sup>, A. Dainese<sup>104</sup>, R. Dang<sup>7</sup>, A. Danu<sup>58</sup>,  
765 D. Das<sup>97</sup>, I. Das<sup>47</sup>, K. Das<sup>97</sup>, S. Das<sup>4</sup>, A. Dash<sup>116</sup>, S. Dash<sup>44</sup>, S. De<sup>126</sup>, H. Delagrange<sup>109,i</sup>, A. Deloff<sup>73</sup>,  
766 E. Dénes<sup>130</sup>, G. D’Erasmus<sup>31</sup>, A. De Caro<sup>29,12</sup>, G. de Cataldo<sup>100</sup>, J. de Cuveland<sup>39</sup>, A. De Falco<sup>23</sup>,  
767 D. De Gruttola<sup>12,29</sup>, N. De Marco<sup>107</sup>, S. De Pasquale<sup>29</sup>, R. de Rooij<sup>53</sup>, M.A. Diaz Corchero<sup>10</sup>, T. Dietel<sup>85,50</sup>,  
768 P. Dillenseger<sup>49</sup>, R. Diviá<sup>34</sup>, D. Di Bari<sup>31</sup>, S. Di Liberto<sup>105</sup>, A. Di Mauro<sup>34</sup>, P. Di Nezza<sup>68</sup>, Ø. Djuvslund<sup>17</sup>,  
769 A. Dobrin<sup>53</sup>, T. Dobrowolski<sup>73</sup>, D. Domenicis Gimenez<sup>115</sup>, B. Dönigus<sup>49</sup>, O. Dordic<sup>21</sup>, S. Dørheim<sup>88</sup>,  
770 A.K. Dubey<sup>126</sup>, A. Dubla<sup>53</sup>, L. Ducroux<sup>124</sup>, P. Dupieux<sup>66</sup>, A.K. Dutta Majumdar<sup>97</sup>, T. E. Hilden<sup>42</sup>,  
771 R.J. Ehlers<sup>131</sup>, D. Elia<sup>100</sup>, H. Engel<sup>48</sup>, B. Erazmus<sup>109,34</sup>, H.A. Erdal<sup>35</sup>, D. Eschweiler<sup>39</sup>, B. Espagnon<sup>47</sup>,  
772 M. Esposito<sup>34</sup>, M. Estienne<sup>109</sup>, S. Esumi<sup>122</sup>, D. Evans<sup>98</sup>, S. Evdokimov<sup>108</sup>, D. Fabris<sup>104</sup>, J. Faivre<sup>67</sup>,  
773 D. Falchieri<sup>26</sup>, A. Fantoni<sup>68</sup>, M. Fasel<sup>89,70</sup>, D. Fehlinger<sup>17</sup>, L. Feldkamp<sup>50</sup>, D. Felea<sup>58</sup>, A. Feliciello<sup>107</sup>,  
774 G. Feofilov<sup>125</sup>, J. Ferencei<sup>79</sup>, A. Fernández Téllez<sup>2</sup>, E.G. Ferreira<sup>16</sup>, A. Ferretti<sup>25</sup>, A. Festanti<sup>28</sup>, J. Figiel<sup>112</sup>,  
775 M.A.S. Figueredo<sup>119</sup>, S. Filchagin<sup>95</sup>, D. Finogeev<sup>52</sup>, F.M. Fionda<sup>31</sup>, E.M. Fiore<sup>31</sup>, E. Floratos<sup>84</sup>, M. Floris<sup>34</sup>,  
776 S. Foertsch<sup>61</sup>, P. Foka<sup>93</sup>, S. Fokin<sup>96</sup>, E. Fragiaco<sup>106</sup>, A. Francescon<sup>28,34</sup>, U. Frankenfeld<sup>93</sup>, U. Fuchs<sup>34</sup>,  
777 C. Furget<sup>67</sup>, A. Furs<sup>52</sup>, M. Fusco Girard<sup>29</sup>, J.J. Gaardhøje<sup>76</sup>, M. Gagliardi<sup>25</sup>, A.M. Gago<sup>99</sup>, M. Gallio<sup>25</sup>,  
778 D.R. Gangadharan<sup>70,19</sup>, P. Ganoti<sup>80,84</sup>, C. Gao<sup>7</sup>, C. Garabatos<sup>93</sup>, E. Garcia-Solis<sup>13</sup>, C. Gargiulo<sup>34</sup>,  
779 I. Garishvili<sup>71</sup>, J. Gerhard<sup>39</sup>, M. Germain<sup>109</sup>, A. Gheata<sup>34</sup>, M. Gheata<sup>34,58</sup>, B. Ghidini<sup>31</sup>, P. Ghosh<sup>126</sup>,  
780 S.K. Ghosh<sup>4</sup>, P. Gianotti<sup>68</sup>, P. Giubellino<sup>34</sup>, E. Gladysz-Dziadus<sup>112</sup>, P. Glässel<sup>89</sup>, A. Gomez Ramirez<sup>48</sup>,  
781 P. González-Zamora<sup>10</sup>, S. Gorbunov<sup>39</sup>, L. Görlich<sup>112</sup>, S. Gotovac<sup>111</sup>, L.K. Graczykowski<sup>128</sup>, A. Grelli<sup>53</sup>,  
782 A. Grigoras<sup>34</sup>, C. Grigoras<sup>34</sup>, V. Grigoriev<sup>72</sup>, A. Grigoryan<sup>1</sup>, S. Grigoryan<sup>62</sup>, B. Grinyov<sup>3</sup>, N. Grion<sup>106</sup>,  
783 J.F. Grosse-Oetringhaus<sup>34</sup>, J.-Y. Grossiord<sup>124</sup>, R. Grosso<sup>34</sup>, F. Guber<sup>52</sup>, R. Guernane<sup>67</sup>, B. Guerzoni<sup>26</sup>,  
784 M. Guilbaud<sup>124</sup>, K. Gulbrandsen<sup>76</sup>, H. Gulkanyan<sup>1</sup>, M. Gumbo<sup>85</sup>, T. Gunji<sup>121</sup>, A. Gupta<sup>86</sup>, R. Gupta<sup>86</sup>,  
785 K. H. Khan<sup>15</sup>, R. Haake<sup>50</sup>, Ø. Haaland<sup>17</sup>, C. Hadjidakis<sup>47</sup>, M. Haiduc<sup>58</sup>, H. Hamagaki<sup>121</sup>, G. Hamar<sup>130</sup>,  
786 L.D. Hanratty<sup>98</sup>, A. Hansen<sup>76</sup>, J.W. Harris<sup>131</sup>, H. Hartmann<sup>39</sup>, A. Harton<sup>13</sup>, D. Hatzifotiadou<sup>101</sup>,  
787 S. Hayashi<sup>121</sup>, S.T. Heckel<sup>49</sup>, M. Heide<sup>50</sup>, H. Helstrup<sup>35</sup>, A. Herghelegiu<sup>74</sup>, G. Herrera Corral<sup>11</sup>, B.A. Hess<sup>33</sup>,  
788 K.F. Hetland<sup>35</sup>, B. Hippolyte<sup>51</sup>, J. Hladky<sup>56</sup>, P. Hristov<sup>34</sup>, M. Huang<sup>17</sup>, T.J. Humanic<sup>19</sup>, N. Hussain<sup>41</sup>,  
789 T. Hussain<sup>18</sup>, D. Hutter<sup>39</sup>, D.S. Hwang<sup>20</sup>, R. Ilkaev<sup>95</sup>, I. Ilkiv<sup>73</sup>, M. Inaba<sup>122</sup>, G.M. Innocenti<sup>25</sup>, C. Ionita<sup>34</sup>,

790 M. Ippolitov<sup>96</sup>, M. Irfan<sup>18</sup>, M. Ivanov<sup>93</sup>, V. Ivanov<sup>81</sup>, A. Jachołkowski<sup>27</sup>, P.M. Jacobs<sup>70</sup>, C. Jahnke<sup>115</sup>,  
 791 H.J. Jang<sup>64</sup>, M.A. Janik<sup>128</sup>, P.H.S.Y. Jayarathna<sup>117</sup>, C. Jena<sup>28</sup>, S. Jena<sup>117</sup>, R.T. Jimenez Bustamante<sup>59</sup>,  
 792 P.G. Jones<sup>98</sup>, H. Jung<sup>40</sup>, A. Jusko<sup>98</sup>, V. Kadysheskiy<sup>62</sup>, P. Kalinak<sup>55</sup>, A. Kalweit<sup>34</sup>, J. Kamin<sup>49</sup>, J.H. Kang<sup>132</sup>,  
 793 V. Kaplin<sup>72</sup>, S. Kar<sup>126</sup>, A. Karasu Uysal<sup>65</sup>, O. Karavichev<sup>52</sup>, T. Karavicheva<sup>52</sup>, E. Karpechev<sup>52</sup>,  
 794 U. Keschull<sup>48</sup>, R. Keidel<sup>133</sup>, D.L.D. Keijdener<sup>53</sup>, M. Keil<sup>SVN34</sup>, M.M. Khan<sup>iii.18</sup>, P. Khan<sup>97</sup>, S.A. Khan<sup>126</sup>,  
 795 A. Khanzadeev<sup>81</sup>, Y. Kharlov<sup>108</sup>, B. Kileng<sup>35</sup>, B. Kim<sup>132</sup>, D.W. Kim<sup>40.64</sup>, D.J. Kim<sup>118</sup>, J.S. Kim<sup>40</sup>, M. Kim<sup>40</sup>,  
 796 M. Kim<sup>132</sup>, S. Kim<sup>20</sup>, T. Kim<sup>132</sup>, S. Kirsch<sup>39</sup>, I. Kisel<sup>39</sup>, S. Kiselev<sup>54</sup>, A. Kisiel<sup>128</sup>, G. Kiss<sup>130</sup>, J.L. Klay<sup>6</sup>,  
 797 J. Klein<sup>89</sup>, C. Klein-Bösing<sup>50</sup>, A. Kluge<sup>34</sup>, M.L. Knichel<sup>93</sup>, A.G. Knospe<sup>113</sup>, C. Kobdaj<sup>110.34</sup>, M. Kofarago<sup>34</sup>,  
 798 M.K. Köhler<sup>93</sup>, T. Kollegger<sup>39</sup>, A. Kolojvari<sup>125</sup>, V. Kondratiev<sup>125</sup>, N. Kondratyeva<sup>72</sup>, A. Konevskikh<sup>52</sup>,  
 799 V. Kovalenko<sup>125</sup>, M. Kowalski<sup>112</sup>, S. Kox<sup>67</sup>, G. Koyithatta Meethalevedu<sup>44</sup>, J. Kral<sup>118</sup>, I. Králik<sup>55</sup>,  
 800 A. Kravčáková<sup>38</sup>, M. Krelina<sup>37</sup>, M. Kretz<sup>39</sup>, M. Krivda<sup>55.98</sup>, F. Krizek<sup>79</sup>, E. Kryshen<sup>34</sup>, M. Krzewicki<sup>93.39</sup>,  
 801 V. Kučera<sup>79</sup>, Y. Kucheriaev<sup>96.i</sup>, T. Kugathasan<sup>34</sup>, C. Kuhn<sup>51</sup>, P.G. Kuijer<sup>77</sup>, I. Kulakov<sup>49</sup>, J. Kumar<sup>44</sup>,  
 802 P. Kurashvili<sup>73</sup>, A. Kurepin<sup>52</sup>, A.B. Kurepin<sup>52</sup>, A. Kuryakin<sup>95</sup>, S. Kushpil<sup>79</sup>, M.J. Kweon<sup>89.46</sup>, Y. Kwon<sup>132</sup>,  
 803 P. Ladron de Guevara<sup>59</sup>, C. Lagana Fernandes<sup>115</sup>, I. Lakomov<sup>47</sup>, R. Langoy<sup>127</sup>, C. Lara<sup>48</sup>, A. Lardeux<sup>109</sup>,  
 804 A. Lattuca<sup>25</sup>, S.L. La Pointe<sup>107</sup>, P. La Rocca<sup>27</sup>, R. Lea<sup>24</sup>, L. Leardini<sup>89</sup>, G.R. Lee<sup>98</sup>, I. Legrand<sup>34</sup>, J. Lehnert<sup>49</sup>,  
 805 R.C. Lemmon<sup>78</sup>, V. Lenti<sup>100</sup>, E. Leogrande<sup>53</sup>, M. Leoncino<sup>25</sup>, I. León Monzón<sup>114</sup>, P. Lévai<sup>130</sup>, S. Li<sup>7.66</sup>,  
 806 J. Lien<sup>127</sup>, R. Lietava<sup>98</sup>, S. Lindal<sup>21</sup>, V. Lindenstruth<sup>39</sup>, C. Lippmann<sup>93</sup>, M.A. Lisa<sup>19</sup>, H.M. Ljunggren<sup>32</sup>,  
 807 D.F. Lodato<sup>53</sup>, P.I. Loenne<sup>17</sup>, V.R. Loggins<sup>129</sup>, V. Loginov<sup>72</sup>, D. Lohner<sup>89</sup>, C. Loizides<sup>70</sup>, X. Lopez<sup>66</sup>,  
 808 E. López Torres<sup>9</sup>, X.-G. Lu<sup>89</sup>, P. Luettig<sup>49</sup>, M. Lunardon<sup>28</sup>, G. Luparello<sup>53.24</sup>, R. Ma<sup>131</sup>, A. Maevskaya<sup>52</sup>,  
 809 M. Mager<sup>34</sup>, D.P. Mahapatra<sup>57</sup>, S.M. Mahmood<sup>21</sup>, A. Maire<sup>51.89</sup>, R.D. Majka<sup>131</sup>, M. Malaev<sup>81</sup>,  
 810 I. Maldonado Cervantes<sup>59</sup>, L. Malinina<sup>iv.62</sup>, D. Mal'Kevich<sup>54</sup>, P. Malzacher<sup>93</sup>, A. Mamonov<sup>95</sup>, L. Manceau<sup>107</sup>,  
 811 V. Manko<sup>96</sup>, F. Manso<sup>66</sup>, V. Manzari<sup>100</sup>, M. Marchisone<sup>66.25</sup>, J. Mareš<sup>56</sup>, G.V. Margagliotti<sup>24</sup>, A. Margotti<sup>101</sup>,  
 812 A. Marín<sup>93</sup>, C. Markert<sup>34.113</sup>, M. Marquard<sup>49</sup>, I. Martashvili<sup>120</sup>, N.A. Martin<sup>93</sup>, P. Martinengo<sup>34</sup>,  
 813 M.I. Martínez<sup>2</sup>, G. Martínez García<sup>109</sup>, J. Martin Blanco<sup>109</sup>, Y. Martynov<sup>3</sup>, A. Mas<sup>109</sup>, S. Masciocchi<sup>93</sup>,  
 814 M. Maserà<sup>25</sup>, A. Masoni<sup>102</sup>, L. Massacrier<sup>109</sup>, A. Mastroserio<sup>31</sup>, A. Matyja<sup>112</sup>, C. Mayer<sup>112</sup>, J. Mazer<sup>120</sup>,  
 815 M.A. Mazzoni<sup>105</sup>, D. McDonald<sup>117</sup>, F. Meddi<sup>22</sup>, A. Menchaca-Rocha<sup>60</sup>, E. Meninno<sup>29</sup>, J. Mercado Pérez<sup>89</sup>,  
 816 M. Meres<sup>36</sup>, Y. Miake<sup>122</sup>, K. Mikhaylov<sup>54.62</sup>, L. Milano<sup>34</sup>, J. Milosevic<sup>v.21</sup>, A. Mischke<sup>53</sup>, A.N. Mishra<sup>45</sup>,  
 817 D. Miśkowiec<sup>93</sup>, J. Mitra<sup>126</sup>, C.M. Mitu<sup>58</sup>, J. Mlynar<sup>129</sup>, N. Mohammadi<sup>53</sup>, B. Mohanty<sup>126.75</sup>, L. Molnar<sup>51</sup>,  
 818 L. Montaña Zetina<sup>11</sup>, E. Montes<sup>10</sup>, M. Morando<sup>28</sup>, D.A. Moreira De Godoy<sup>109.115</sup>, S. Moretto<sup>28</sup>,  
 819 A. Morreale<sup>109</sup>, A. Morsch<sup>34</sup>, V. Muccifora<sup>68</sup>, E. Mudnic<sup>111</sup>, D. Mühlheim<sup>50</sup>, S. Muhuri<sup>126</sup>, M. Mukherjee<sup>126</sup>,  
 820 H. Müller<sup>34</sup>, M.G. Munhoz<sup>115</sup>, S. Murray<sup>85</sup>, L. Musa<sup>34</sup>, J. Musinsky<sup>55</sup>, B.K. Nandi<sup>44</sup>, R. Nania<sup>101</sup>,  
 821 E. Nappi<sup>100</sup>, C. Nattrass<sup>120</sup>, K. Nayak<sup>75</sup>, T.K. Nayak<sup>126</sup>, S. Nazarenko<sup>95</sup>, A. Nedosekin<sup>54</sup>, M. Nicassio<sup>93</sup>,  
 822 M. Niculescu<sup>34.58</sup>, J. Niedziela<sup>34</sup>, B.S. Nielsen<sup>76</sup>, S. Nikolaev<sup>96</sup>, S. Nikulin<sup>96</sup>, V. Nikulin<sup>81</sup>, B.S. Nilsen<sup>82</sup>,  
 823 F. Noferini<sup>12.101</sup>, P. Nomokonov<sup>62</sup>, G. Nooren<sup>53</sup>, J. Norman<sup>119</sup>, A. Nyanin<sup>96</sup>, J. Nystrand<sup>17</sup>, H. Oeschler<sup>89</sup>,  
 824 S. Oh<sup>131</sup>, S.K. Oh<sup>vi.63.40</sup>, A. Okatan<sup>65</sup>, T. Okubo<sup>43</sup>, L. Olah<sup>130</sup>, J. Oleniacz<sup>128</sup>, A.C. Oliveira Da Silva<sup>115</sup>,  
 825 J. Onderwaater<sup>93</sup>, C. Oppedisano<sup>107</sup>, A. Ortiz Velasquez<sup>32.59</sup>, A. Oskarsson<sup>32</sup>, J. Otwinowski<sup>112.93</sup>,  
 826 K. Oyama<sup>89</sup>, M. Ozdemir<sup>49</sup>, P. Sahoo<sup>45</sup>, Y. Pachmayer<sup>89</sup>, M. Pachr<sup>37</sup>, P. Pagano<sup>29</sup>, G. Paic<sup>59</sup>, C. Pajares<sup>16</sup>,  
 827 S.K. Pal<sup>126</sup>, A. Palmeri<sup>103</sup>, D. Pant<sup>44</sup>, V. Papikyan<sup>1</sup>, G.S. Pappalardo<sup>103</sup>, P. Pareek<sup>45</sup>, W.J. Park<sup>93</sup>, S. Parmar<sup>83</sup>,  
 828 A. Passfeld<sup>50</sup>, D.I. Patalakha<sup>108</sup>, V. Paticchio<sup>100</sup>, B. Paul<sup>97</sup>, T. Pawlak<sup>128</sup>, T. Peitzmann<sup>53</sup>,  
 829 H. Pereira Da Costa<sup>14</sup>, E. Pereira De Oliveira Filho<sup>115</sup>, D. Peresunko<sup>96</sup>, C.E. Pérez Lara<sup>77</sup>, A. Pesci<sup>101</sup>,  
 830 V. Peskov<sup>49</sup>, Y. Pestov<sup>5</sup>, V. Petráček<sup>37</sup>, M. Petran<sup>37</sup>, M. Petris<sup>74</sup>, M. Petrovici<sup>74</sup>, C. Petta<sup>27</sup>, S. Piano<sup>106</sup>,  
 831 M. Pikna<sup>36</sup>, P. Pillot<sup>109</sup>, O. Pinazza<sup>101.34</sup>, L. Pinsky<sup>117</sup>, D.B. Piyarathna<sup>117</sup>, M. Płoski<sup>70</sup>, M. Planinic<sup>94.123</sup>,  
 832 J. Pluta<sup>128</sup>, S. Pochybova<sup>130</sup>, P.L.M. Podesta-Lerma<sup>114</sup>, M.G. Poghosyan<sup>82.34</sup>, E.H.O. Pohjoisaho<sup>42</sup>,  
 833 B. Polichtchouk<sup>108</sup>, N. Poljak<sup>123.94</sup>, A. Pop<sup>74</sup>, S. Porteboeuf-Houssais<sup>66</sup>, J. Porter<sup>70</sup>, B. Potukuchi<sup>86</sup>,  
 834 S.K. Prasad<sup>129.4</sup>, R. Preghenella<sup>101.12</sup>, F. Prino<sup>107</sup>, C.A. Pruneau<sup>129</sup>, I. Pshenichnov<sup>52</sup>, M. Puccio<sup>107</sup>,  
 835 G. Puddu<sup>23</sup>, P. Pujahari<sup>129</sup>, V. Punin<sup>95</sup>, J. Putschke<sup>129</sup>, H. Qvigstad<sup>21</sup>, A. Rachevski<sup>106</sup>, S. Raha<sup>4</sup>, S. Rajput<sup>86</sup>,  
 836 J. Rak<sup>118</sup>, A. Rakotozafindrabe<sup>14</sup>, L. Ramello<sup>30</sup>, R. Raniwala<sup>87</sup>, S. Raniwala<sup>87</sup>, S.S. Räsänen<sup>42</sup>,  
 837 B.T. Rascanu<sup>49</sup>, D. Rathee<sup>83</sup>, A.W. Rauf<sup>15</sup>, V. Razazi<sup>23</sup>, K.F. Read<sup>120</sup>, J.S. Real<sup>67</sup>, K. Redlich<sup>vii.73</sup>,  
 838 R.J. Reed<sup>131.129</sup>, A. Rehman<sup>17</sup>, P. Reichelt<sup>49</sup>, M. Reicher<sup>53</sup>, F. Reidt<sup>89.34</sup>, R. Renfordt<sup>49</sup>, A.R. Reolon<sup>68</sup>,  
 839 A. Reshetin<sup>52</sup>, F. Rettig<sup>39</sup>, J.-P. Revol<sup>34</sup>, K. Reygers<sup>89</sup>, V. Riabov<sup>81</sup>, R.A. Ricci<sup>69</sup>, T. Richert<sup>32</sup>, M. Richter<sup>21</sup>,  
 840 P. Riedler<sup>34</sup>, W. Riegler<sup>34</sup>, F. Riggi<sup>27</sup>, A. Rivetti<sup>107</sup>, E. Rocco<sup>53</sup>, M. Rodríguez Cahuantzi<sup>2</sup>,  
 841 A. Rodríguez Manso<sup>77</sup>, K. Røed<sup>21</sup>, E. Rogochaya<sup>62</sup>, S. Rohni<sup>86</sup>, D. Rohr<sup>39</sup>, D. Röhrich<sup>17</sup>, R. Romita<sup>78.119</sup>,  
 842 F. Ronchetti<sup>68</sup>, L. Ronflette<sup>109</sup>, P. Rosnet<sup>66</sup>, A. Rossi<sup>34</sup>, F. Roukoutakis<sup>84</sup>, A. Roy<sup>45</sup>, C. Roy<sup>51</sup>, P. Roy<sup>97</sup>,  
 843 A.J. Rubio Montero<sup>10</sup>, R. Rui<sup>24</sup>, R. Russo<sup>25</sup>, E. Ryabinkin<sup>96</sup>, Y. Ryabov<sup>81</sup>, A. Rybicki<sup>112</sup>, S. Sadovsky<sup>108</sup>,  
 844 K. Šafařík<sup>34</sup>, B. Sahlmüller<sup>49</sup>, R. Sahoo<sup>45</sup>, S. Sahoo<sup>57</sup>, P.K. Sahu<sup>57</sup>, J. Saini<sup>126</sup>, S. Sakai<sup>68</sup>, C.A. Salgado<sup>16</sup>,  
 845 J. Salzwedel<sup>19</sup>, S. Sambyal<sup>86</sup>, V. Samsonov<sup>81</sup>, X. Sanchez Castro<sup>51</sup>, F.J. Sánchez Rodríguez<sup>114</sup>, L. Šándor<sup>55</sup>,

846 A. Sandoval<sup>60</sup>, M. Sano<sup>122</sup>, G. Santagati<sup>27</sup>, D. Sarkar<sup>126</sup>, E. Scapparone<sup>101</sup>, F. Scarlassara<sup>28</sup>,  
847 R.P. Scharenberg<sup>91</sup>, C. Schiaua<sup>74</sup>, R. Schicker<sup>89</sup>, C. Schmidt<sup>93</sup>, H.R. Schmidt<sup>33</sup>, S. Schuchmann<sup>49</sup>,  
848 J. Schukraft<sup>34</sup>, M. Schulc<sup>37</sup>, T. Schuster<sup>131</sup>, Y. Schutz<sup>34,109</sup>, K. Schwarz<sup>93</sup>, K. Schweda<sup>93</sup>, G. Scioli<sup>26</sup>,  
849 E. Scomparin<sup>107</sup>, R. Scott<sup>120</sup>, G. Segato<sup>28</sup>, J.E. Seger<sup>82</sup>, Y. Sekiguchi<sup>121</sup>, I. Selyuzhenkov<sup>93</sup>, K. Senosi<sup>61</sup>,  
850 J. Seo<sup>92</sup>, E. Serradilla<sup>10,60</sup>, A. Sevcenco<sup>58</sup>, A. Shabetai<sup>109</sup>, G. Shabratova<sup>62</sup>, R. Shahoyan<sup>34</sup>,  
851 A. Shangaraev<sup>108</sup>, A. Sharma<sup>86</sup>, N. Sharma<sup>120</sup>, S. Sharma<sup>86</sup>, K. Shigaki<sup>43</sup>, K. Shtejer<sup>9,25</sup>, Y. Sibiriak<sup>96</sup>,  
852 S. Siddhanta<sup>102</sup>, T. Siemiarzuk<sup>73</sup>, D. Silvermyr<sup>80</sup>, C. Silvestre<sup>67</sup>, G. Simatovic<sup>123</sup>, R. Singaraju<sup>126</sup>,  
853 R. Singh<sup>86</sup>, S. Singha<sup>75,126</sup>, V. Singhal<sup>126</sup>, B.C. Sinha<sup>126</sup>, T. Sinha<sup>97</sup>, B. Sitar<sup>36</sup>, M. Sitta<sup>30</sup>, T.B. Skaali<sup>21</sup>,  
854 K. Skjerdal<sup>17</sup>, M. Slupecki<sup>118</sup>, N. Smirnov<sup>131</sup>, R.J.M. Snellings<sup>53</sup>, C. Sogaard<sup>32</sup>, R. Soltz<sup>71</sup>, J. Song<sup>92</sup>,  
855 M. Song<sup>132</sup>, F. Soramel<sup>28</sup>, S. Sorensen<sup>120</sup>, M. Spacek<sup>37</sup>, E. Spiriti<sup>68</sup>, I. Sputowska<sup>112</sup>,  
856 M. Spyropoulou-Stassinaki<sup>84</sup>, B.K. Srivastava<sup>91</sup>, J. Stachel<sup>89</sup>, I. Stan<sup>58</sup>, G. Stefanek<sup>73</sup>, M. Steinpreis<sup>19</sup>,  
857 E. Stenlund<sup>32</sup>, G. Steyn<sup>61</sup>, J.H. Stiller<sup>89</sup>, D. Stocco<sup>109</sup>, M. Stolpovskiy<sup>108</sup>, P. Strmen<sup>36</sup>, A.A.P. Suaide<sup>115</sup>,  
858 T. Sugitate<sup>43</sup>, C. Suire<sup>47</sup>, M. Suleymanov<sup>15</sup>, R. Sultanov<sup>54</sup>, M. Šumbera<sup>79</sup>, T.J.M. Symons<sup>70</sup>, A. Szabo<sup>36</sup>,  
859 A. Szanto de Toledo<sup>115</sup>, I. Szarka<sup>36</sup>, A. Szczepankiewicz<sup>34</sup>, M. Szymanski<sup>128</sup>, J. Takahashi<sup>116</sup>,  
860 M.A. Tangaro<sup>31</sup>, J.D. Tapia Takaki<sup>viii,47</sup>, A. Tarantola Peloni<sup>49</sup>, A. Tarazona Martinez<sup>34</sup>, M. Tariq<sup>18</sup>,  
861 M.G. Tarzila<sup>74</sup>, A. Tauro<sup>34</sup>, G. Tejada Muñoz<sup>2</sup>, A. Telesca<sup>34</sup>, K. Terasaki<sup>121</sup>, C. Terrevoli<sup>23</sup>, J. Thäder<sup>93</sup>,  
862 D. Thomas<sup>53</sup>, R. Tieulent<sup>124</sup>, A.R. Timmins<sup>117</sup>, A. Toia<sup>49,104</sup>, V. Trubnikov<sup>3</sup>, W.H. Trzaska<sup>118</sup>, T. Tsuji<sup>121</sup>,  
863 A. Tumkin<sup>95</sup>, R. Turrisi<sup>104</sup>, T.S. Tveter<sup>21</sup>, K. Ullaland<sup>17</sup>, A. Uras<sup>124</sup>, G.L. Usai<sup>23</sup>, M. Vajzer<sup>79</sup>, M. Vala<sup>55,62</sup>,  
864 L. Valencia Palomo<sup>66</sup>, S. Vallero<sup>25,89</sup>, P. Vande Vyvre<sup>34</sup>, J. Van Der Maarel<sup>53</sup>, J.W. Van Hoorne<sup>34</sup>,  
865 M. van Leeuwen<sup>53</sup>, A. Vargas<sup>2</sup>, M. Vargyas<sup>118</sup>, R. Varma<sup>44</sup>, M. Vasileiou<sup>84</sup>, A. Vasiliev<sup>96</sup>, V. Vechernin<sup>125</sup>,  
866 M. Veldhoen<sup>53</sup>, A. Velure<sup>17</sup>, M. Venaruzzo<sup>69,24</sup>, E. Vercellin<sup>25</sup>, S. Vergara Limón<sup>2</sup>, R. Vernet<sup>8</sup>, M. Verweij<sup>129</sup>,  
867 L. Vickovic<sup>111</sup>, G. Viesti<sup>28</sup>, J. Viinikainen<sup>118</sup>, Z. Vilakazi<sup>61</sup>, O. Villalobos Baillie<sup>98</sup>, A. Vinogradov<sup>96</sup>,  
868 L. Vinogradov<sup>125</sup>, Y. Vinogradov<sup>95</sup>, T. Virgili<sup>29</sup>, V. Vislavicius<sup>32</sup>, Y.P. Viyogi<sup>126</sup>, A. Vodopyanov<sup>62</sup>,  
869 M.A. Völkl<sup>89</sup>, K. Voloshin<sup>54</sup>, S.A. Voloshin<sup>129</sup>, G. Volpe<sup>34</sup>, B. von Haller<sup>34</sup>, I. Vorobyev<sup>125</sup>, D. Vranic<sup>34,93</sup>,  
870 J. Vrláková<sup>38</sup>, B. Vulpesu<sup>66</sup>, A. Vyushin<sup>95</sup>, B. Wagner<sup>17</sup>, J. Wagner<sup>93</sup>, V. Wagner<sup>37</sup>, M. Wang<sup>7,109</sup>,  
871 Y. Wang<sup>89</sup>, D. Watanabe<sup>122</sup>, M. Weber<sup>117,34</sup>, S.G. Weber<sup>93</sup>, J.P. Wessels<sup>50</sup>, U. Westerhoff<sup>50</sup>, J. Wiechula<sup>33</sup>,  
872 J. Wikne<sup>21</sup>, M. Wilde<sup>50</sup>, G. Wilk<sup>73</sup>, J. Wilkinson<sup>89</sup>, M.C.S. Williams<sup>101</sup>, B. Windelband<sup>89</sup>, M. Winn<sup>89</sup>,  
873 C.G. Yaldo<sup>129</sup>, Y. Yamaguchi<sup>121</sup>, H. Yang<sup>53</sup>, P. Yang<sup>7</sup>, S. Yang<sup>17</sup>, S. Yano<sup>43</sup>, S. Yasnopolskiy<sup>96</sup>, J. Yi<sup>92</sup>,  
874 Z. Yin<sup>7</sup>, I.-K. Yoo<sup>92</sup>, I. Yushmanov<sup>96</sup>, A. Zaborowska<sup>128</sup>, V. Zaccolo<sup>76</sup>, A. Zaman<sup>15</sup>, C. Zampolli<sup>101</sup>,  
875 S. Zaporozhets<sup>62</sup>, A. Zarochentsev<sup>125</sup>, P. Závada<sup>56</sup>, N. Zaviyalov<sup>95</sup>, H. Zbroszczyk<sup>128</sup>, I.S. Zgura<sup>58</sup>,  
876 M. Zhalov<sup>81</sup>, H. Zhang<sup>7</sup>, X. Zhang<sup>7,70</sup>, Y. Zhang<sup>7</sup>, C. Zhao<sup>21</sup>, N. Zhigareva<sup>54</sup>, D. Zhou<sup>7</sup>, F. Zhou<sup>7</sup>,  
877 Y. Zhou<sup>53</sup>, Zhou, Zhuo<sup>17</sup>, H. Zhu<sup>7</sup>, J. Zhu<sup>7,109</sup>, X. Zhu<sup>7</sup>, A. Zichichi<sup>12,26</sup>, A. Zimmermann<sup>89</sup>,  
878 M.B. Zimmermann<sup>50,34</sup>, G. Zinovjev<sup>3</sup>, Y. Zoccarato<sup>124</sup>, M. Zyzak<sup>49</sup>

## 879 Affiliation notes

- 880 <sup>i</sup> Deceased  
881 <sup>ii</sup> Also at: St. Petersburg State Polytechnical University  
882 <sup>iii</sup> Also at: Department of Applied Physics, Aligarh Muslim University, Aligarh, India  
883 <sup>iv</sup> Also at: M.V. Lomonosov Moscow State University, D.V. Skobeltsyn Institute of Nuclear Physics,  
884 Moscow, Russia  
885 <sup>v</sup> Also at: University of Belgrade, Faculty of Physics and "Vinča" Institute of Nuclear Sciences, Belgrade,  
886 Serbia  
887 <sup>vi</sup> Permanent Address: Permanent Address: Konkuk University, Seoul, Korea  
888 <sup>vii</sup> Also at: Institute of Theoretical Physics, University of Wrocław, Wrocław, Poland  
889 <sup>viii</sup> Also at: University of Kansas, Lawrence, KS, United States

## 890 Collaboration Institutes

- 891 <sup>1</sup> A.I. Alikhanyan National Science Laboratory (Yerevan Physics Institute) Foundation, Yerevan, Armenia  
892 <sup>2</sup> Benemérita Universidad Autónoma de Puebla, Puebla, Mexico  
893 <sup>3</sup> Bogolyubov Institute for Theoretical Physics, Kiev, Ukraine  
894 <sup>4</sup> Bose Institute, Department of Physics and Centre for Astroparticle Physics and Space Science (CAPSS),  
895 Kolkata, India  
896 <sup>5</sup> Budker Institute for Nuclear Physics, Novosibirsk, Russia  
897 <sup>6</sup> California Polytechnic State University, San Luis Obispo, CA, United States  
898 <sup>7</sup> Central China Normal University, Wuhan, China

- 899 8 Centre de Calcul de l'IN2P3, Villeurbanne, France  
900 9 Centro de Aplicaciones Tecnológicas y Desarrollo Nuclear (CEADEN), Havana, Cuba  
901 10 Centro de Investigaciones Energéticas Medioambientales y Tecnológicas (CIEMAT), Madrid, Spain  
902 11 Centro de Investigación y de Estudios Avanzados (CINVESTAV), Mexico City and Mérida, Mexico  
903 12 Centro Fermi - Museo Storico della Fisica e Centro Studi e Ricerche "Enrico Fermi", Rome, Italy  
904 13 Chicago State University, Chicago, USA  
905 14 Commissariat à l'Energie Atomique, IRFU, Saclay, France  
906 15 COMSATS Institute of Information Technology (CIIT), Islamabad, Pakistan  
907 16 Departamento de Física de Partículas and IGFAE, Universidad de Santiago de Compostela, Santiago de  
908 Compostela, Spain  
909 17 Department of Physics and Technology, University of Bergen, Bergen, Norway  
910 18 Department of Physics, Aligarh Muslim University, Aligarh, India  
911 19 Department of Physics, Ohio State University, Columbus, OH, United States  
912 20 Department of Physics, Sejong University, Seoul, South Korea  
913 21 Department of Physics, University of Oslo, Oslo, Norway  
914 22 Dipartimento di Fisica dell'Università 'La Sapienza' and Sezione INFN Rome, Italy  
915 23 Dipartimento di Fisica dell'Università and Sezione INFN, Cagliari, Italy  
916 24 Dipartimento di Fisica dell'Università and Sezione INFN, Trieste, Italy  
917 25 Dipartimento di Fisica dell'Università and Sezione INFN, Turin, Italy  
918 26 Dipartimento di Fisica e Astronomia dell'Università and Sezione INFN, Bologna, Italy  
919 27 Dipartimento di Fisica e Astronomia dell'Università and Sezione INFN, Catania, Italy  
920 28 Dipartimento di Fisica e Astronomia dell'Università and Sezione INFN, Padova, Italy  
921 29 Dipartimento di Fisica 'E.R. Caianiello' dell'Università and Gruppo Collegato INFN, Salerno, Italy  
922 30 Dipartimento di Scienze e Innovazione Tecnologica dell'Università del Piemonte Orientale and Gruppo  
923 Collegato INFN, Alessandria, Italy  
924 31 Dipartimento Interateneo di Fisica 'M. Merlin' and Sezione INFN, Bari, Italy  
925 32 Division of Experimental High Energy Physics, University of Lund, Lund, Sweden  
926 33 Eberhard Karls Universität Tübingen, Tübingen, Germany  
927 34 European Organization for Nuclear Research (CERN), Geneva, Switzerland  
928 35 Faculty of Engineering, Bergen University College, Bergen, Norway  
929 36 Faculty of Mathematics, Physics and Informatics, Comenius University, Bratislava, Slovakia  
930 37 Faculty of Nuclear Sciences and Physical Engineering, Czech Technical University in Prague, Prague,  
931 Czech Republic  
932 38 Faculty of Science, P.J. Šafárik University, Košice, Slovakia  
933 39 Frankfurt Institute for Advanced Studies, Johann Wolfgang Goethe-Universität Frankfurt, Frankfurt,  
934 Germany  
935 40 Gangneung-Wonju National University, Gangneung, South Korea  
936 41 Gauhati University, Department of Physics, Guwahati, India  
937 42 Helsinki Institute of Physics (HIP), Helsinki, Finland  
938 43 Hiroshima University, Hiroshima, Japan  
939 44 Indian Institute of Technology Bombay (IIT), Mumbai, India  
940 45 Indian Institute of Technology Indore, Indore (IITI), India  
941 46 Inha University, Incheon, South Korea  
942 47 Institut de Physique Nucléaire d'Orsay (IPNO), Université Paris-Sud, CNRS-IN2P3, Orsay, France  
943 48 Institut für Informatik, Johann Wolfgang Goethe-Universität Frankfurt, Frankfurt, Germany  
944 49 Institut für Kernphysik, Johann Wolfgang Goethe-Universität Frankfurt, Frankfurt, Germany  
945 50 Institut für Kernphysik, Westfälische Wilhelms-Universität Münster, Münster, Germany  
946 51 Institut Pluridisciplinaire Hubert Curien (IPHC), Université de Strasbourg, CNRS-IN2P3, Strasbourg,  
947 France  
948 52 Institute for Nuclear Research, Academy of Sciences, Moscow, Russia  
949 53 Institute for Subatomic Physics of Utrecht University, Utrecht, Netherlands  
950 54 Institute for Theoretical and Experimental Physics, Moscow, Russia  
951 55 Institute of Experimental Physics, Slovak Academy of Sciences, Košice, Slovakia  
952 56 Institute of Physics, Academy of Sciences of the Czech Republic, Prague, Czech Republic  
953 57 Institute of Physics, Bhubaneswar, India  
954 58 Institute of Space Science (ISS), Bucharest, Romania

- 955 59 Instituto de Ciencias Nucleares, Universidad Nacional Autónoma de México, Mexico City, Mexico  
956 60 Instituto de Física, Universidad Nacional Autónoma de México, Mexico City, Mexico  
957 61 iThemba LABS, National Research Foundation, Somerset West, South Africa  
958 62 Joint Institute for Nuclear Research (JINR), Dubna, Russia  
959 63 Konkuk University, Seoul, South Korea  
960 64 Korea Institute of Science and Technology Information, Daejeon, South Korea  
961 65 KTO Karatay University, Konya, Turkey  
962 66 Laboratoire de Physique Corpusculaire (LPC), Clermont Université, Université Blaise Pascal,  
963 CNRS-IN2P3, Clermont-Ferrand, France  
964 67 Laboratoire de Physique Subatomique et de Cosmologie, Université Grenoble-Alpes, CNRS-IN2P3,  
965 Grenoble, France  
966 68 Laboratori Nazionali di Frascati, INFN, Frascati, Italy  
967 69 Laboratori Nazionali di Legnaro, INFN, Legnaro, Italy  
968 70 Lawrence Berkeley National Laboratory, Berkeley, CA, United States  
969 71 Lawrence Livermore National Laboratory, Livermore, CA, United States  
970 72 Moscow Engineering Physics Institute, Moscow, Russia  
971 73 National Centre for Nuclear Studies, Warsaw, Poland  
972 74 National Institute for Physics and Nuclear Engineering, Bucharest, Romania  
973 75 National Institute of Science Education and Research, Bhubaneswar, India  
974 76 Niels Bohr Institute, University of Copenhagen, Copenhagen, Denmark  
975 77 Nikhef, National Institute for Subatomic Physics, Amsterdam, Netherlands  
976 78 Nuclear Physics Group, STFC Daresbury Laboratory, Daresbury, United Kingdom  
977 79 Nuclear Physics Institute, Academy of Sciences of the Czech Republic, Řež u Prahy, Czech Republic  
978 80 Oak Ridge National Laboratory, Oak Ridge, TN, United States  
979 81 Petersburg Nuclear Physics Institute, Gatchina, Russia  
980 82 Physics Department, Creighton University, Omaha, NE, United States  
981 83 Physics Department, Panjab University, Chandigarh, India  
982 84 Physics Department, University of Athens, Athens, Greece  
983 85 Physics Department, University of Cape Town, Cape Town, South Africa  
984 86 Physics Department, University of Jammu, Jammu, India  
985 87 Physics Department, University of Rajasthan, Jaipur, India  
986 88 Physik Department, Technische Universität München, Munich, Germany  
987 89 Physikalisches Institut, Ruprecht-Karls-Universität Heidelberg, Heidelberg, Germany  
988 90 Politecnico di Torino, Turin, Italy  
989 91 Purdue University, West Lafayette, IN, United States  
990 92 Pusan National University, Pusan, South Korea  
991 93 Research Division and ExtreMe Matter Institute EMMI, GSI Helmholtzzentrum für  
992 Schwerionenforschung, Darmstadt, Germany  
993 94 Rudjer Bošković Institute, Zagreb, Croatia  
994 95 Russian Federal Nuclear Center (VNIIEF), Sarov, Russia  
995 96 Russian Research Centre Kurchatov Institute, Moscow, Russia  
996 97 Saha Institute of Nuclear Physics, Kolkata, India  
997 98 School of Physics and Astronomy, University of Birmingham, Birmingham, United Kingdom  
998 99 Sección Física, Departamento de Ciencias, Pontificia Universidad Católica del Perú, Lima, Peru  
999 100 Sezione INFN, Bari, Italy  
1000 101 Sezione INFN, Bologna, Italy  
1001 102 Sezione INFN, Cagliari, Italy  
1002 103 Sezione INFN, Catania, Italy  
1003 104 Sezione INFN, Padova, Italy  
1004 105 Sezione INFN, Rome, Italy  
1005 106 Sezione INFN, Trieste, Italy  
1006 107 Sezione INFN, Turin, Italy  
1007 108 SSC IHEP of NRC Kurchatov institute, Protvino, Russia  
1008 109 SUBATECH, Ecole des Mines de Nantes, Université de Nantes, CNRS-IN2P3, Nantes, France  
1009 110 Suranaree University of Technology, Nakhon Ratchasima, Thailand  
1010 111 Technical University of Split FESB, Split, Croatia



- 1011 112 The Henryk Niewodniczanski Institute of Nuclear Physics, Polish Academy of Sciences, Cracow, Poland  
1012 113 The University of Texas at Austin, Physics Department, Austin, TX, USA  
1013 114 Universidad Autónoma de Sinaloa, Culiacán, Mexico  
1014 115 Universidade de São Paulo (USP), São Paulo, Brazil  
1015 116 Universidade Estadual de Campinas (UNICAMP), Campinas, Brazil  
1016 117 University of Houston, Houston, TX, United States  
1017 118 University of Jyväskylä, Jyväskylä, Finland  
1018 119 University of Liverpool, Liverpool, United Kingdom  
1019 120 University of Tennessee, Knoxville, TN, United States  
1020 121 University of Tokyo, Tokyo, Japan  
1021 122 University of Tsukuba, Tsukuba, Japan  
1022 123 University of Zagreb, Zagreb, Croatia  
1023 124 Université de Lyon, Université Lyon 1, CNRS/IN2P3, IPN-Lyon, Villeurbanne, France  
1024 125 V. Fock Institute for Physics, St. Petersburg State University, St. Petersburg, Russia  
1025 126 Variable Energy Cyclotron Centre, Kolkata, India  
1026 127 Vestfold University College, Tonsberg, Norway  
1027 128 Warsaw University of Technology, Warsaw, Poland  
1028 129 Wayne State University, Detroit, MI, United States  
1029 130 Wigner Research Centre for Physics, Hungarian Academy of Sciences, Budapest, Hungary  
1030 131 Yale University, New Haven, CT, United States  
1031 132 Yonsei University, Seoul, South Korea  
1032 133 Zentrum für Technologietransfer und Telekommunikation (ZTT), Fachhochschule Worms, Worms,  
1033 Germany